

https://dspace.org/

SingleCollision Model for NLoS UV Channels Joint Scattering and Reflection Effects

T Wu; F Yang; T Cao; R Yuan; Li Fei ...

https://hdl.handle.net/10539/47458
WOS

Downloaded from a DSpace repository. https://dspace.org/

Single-Collision Model for NLoS UV Channels: Joint Scattering and Reflection Effects

Tianfeng Wu, *Graduate Student Member, IEEE*, Fang Yang, *Senior Member, IEEE*, Tian Cao, *Member, IEEE*, Renzhi Yuan, *Member, IEEE*, Li Fei, Ling Cheng, *Senior Member, IEEE*, Jian Song, *Fellow, IEEE*, Julian Cheng, *Fellow, IEEE*, and Zhu Han, *Fellow, IEEE*

***Abstract*—ultraviolet (UV) communication research has prioritized channel modeling for its critical role in system optimization. Current non-Line-of-Sight (NLoS) UV modeling mainly addresses obstacle-free scenarios and single-obstacle situations: the former manifests constrained applicability at small transceiver elevation angles with obstacle susceptibility, while the latter suffers from high modeling complexity and can only handle one-obstacle scenarios, which pose critical challenges for Internet of Things applications. To overcome these limitations, we propose a single-collision model for short-range NLoS UV channels incorporating both scattering and reflection effects. Initially, the impact of air scattering on the received pulse energy is presented for diverse obstacle situations, where an obstacle-boundary approximation method (OBAM) is developed to reduce the modeling complexity. Besides, the dimensions, coordinates, shapes, orientation angles, and number of obstacles are considered to emulate practical environments. Subsequently, the impact of obstacle reflection on the received pulse energy is investigated for single, double, and multiple obstacle situations. On this basis, we account for certain scenarios where obstacle surfaces comprise multiple subregions, each characterized by distinct reflection coefficients attributed to their varying material compositions. Moreover, we verify the proposed model by comparing it with the Monte-Carlo photon-tracing (MCPT) model and the obstacle-free integral model via simulations. These results demonstrate that the path loss curves obtained by the proposed model exhibit close alignment with those simulated by the MCPT model, while its calculation time is less than 10% that of the MCPT model. Additionally, when obstacle reflection is prominent, the assessment error of the proposed OBAM can be ignored in estimating the path loss of non-LoS (NLoS) UV channels containing obstacles.**

***Index Terms*—Air scattering, non-LoS (NLoS) channel modeling, obstacle reflection, path loss, single-collision model, ultraviolet (UV) communications.**

Received 10 June 2025; revised 7 July 2025; accepted 19 July 2025. Date of publication 28 July 2025; date of current version 9 October 2025. This work was supported in part by the National Key Research and Development Program of China under Grant 2023YFE0110600; in part by the Open Fund Project of Hanjiang National Laboratory under Grant KF2024027; in part by the National Natural Science Foundation of China under Grant 62401433; in part by the NSF under Grant ECCS-2302469 and Grant CMMI-2222810, Toyota; and in part by the Amazon and Japan Science and Technology Agency (JST) Adopting Sustainable Partnerships for Innovative Research Ecosystem (ASPIRE) under Grant JPMJAP2326. *(Corresponding author: Fang Yang.)*

Tianfeng Wu is with the Department of Electronic Engineering, Beijing National Research Center for Information Science and Technology, Tsinghua University, Beijing 100084, China (e-mail: wtf22@mails.tsinghua.edu.cn).

Fang Yang is with the Department of Electronic Engineering, Beijing National Research Center for Information Science and Technology, Tsinghua University, Beijing 100084, China, and also with the State Key Laboratory of Widegap Semiconductor Optoelectronic Materials and Technologies, Beijing 100084, China (e-mail: fangyang@tsinghua.edu.cn).

Tian Cao is with the School of Telecommunications Engineering, Xidian University, Xi'an 710071, China (e-mail: caotian@xidian.edu.cn).

Renzhi Yuan is with the State Key Laboratory of Networking and Switching Technology, Beijing University of Posts and Telecommunications, Beijing 100876, China (e-mail: renzhi.yuan@bupt.edu.cn).

Li Fei is with Hanjiang National Laboratory, Wuhan 430060, China (e-mail: buaafeili@126.com).

Ling Cheng is with the School of Electrical and Information Engineering, University of the Witwatersrand, Johannesburg 2000, South Africa (e-mail: ling.cheng@wits.ac.za).

Jian Song is with the Department of Electronic Engineering, Tsinghua University, Beijing 100084, China, and also with the Shenzhen International Graduate School, Tsinghua University, Shenzhen 518055, China (e-mail: jsong@tsinghua.edu.cn).

Julian Cheng is with the School of Engineering, The University of British Columbia, Kelowna, BC V1V 1V7, Canada (e-mail: julian.cheng@ubc.ca).

Zhu Han is with the Department of Electrical and Computer Engineering, University of Houston, Houston, TX 77004 USA, and also with the Department of Computer Science and Engineering, Kyung Hee University, Seoul 446-701, South Korea (e-mail: hanzhu22@gmail.com).

Digital Object Identifier 10.1109/JIOT.2025.3593362

I. Introduction

CURRENTLY, radio frequency technology is still broadly employed in wireless communication scenarios due to its extensive coverage, resilience to obstruction, and cost-effective deployment [2]. Nevertheless, this technology also encounters critical issues, including spectral congestion and susceptibility to electromagnetic interference (EMI) [3]. To cope with these problems, emerging technological solutions are being actively developed, including higher-frequency bands like millimeter-wave and terahertz communications, as well as optical wireless communications utilizing infrared, visible, or ultraviolet (UV) light [4], [5]. These alternatives offer substantially higher data rates, wider available bandwidth, and, particularly for optical solutions, immunity to radio frequency EMI, positioning them as viable solutions for future high-demand applications [6].

Among these solutions, UV communication demonstrates a distinctive benefit through its intrinsic support for dual-mode propagation, encompassing both Line-of-Sight (LoS) and non-LoS (NLoS) links [7], while the other alternatives mainly rely on LoS links for communications. Moreover, the background noise of UV communication systems adopting the 200-280 nm band can be neglected due to the strong absorption impact of the atmospheric ozone layer, which is a capability unattainable for other optical bands [8]. For these reasons, UV technology can be considered as a transformative approach for establishing reliable and spectrally efficient wireless networks, particularly in demanding applications, such as the Internet of Things (IoT) [9], [10].

2327-4662 © 2025 IEEE. All rights reserved, including rights for text and data mining, and training of artificial intelligence and similar technologies. Personal use is permitted, but republication/redistribution requires IEEE permission.
See https://www.ieee.org/publications/rights/index.html for more information.
Authorized licensed use limited to: University of Witwatersrand. Downloaded on November 06,2025 at 14:42:10 UTC from IEEE Xplore. Restrictions apply.

Presently, research efforts in UV communications primarily focus on several aspects: solar-blind devices, channel modeling, modulation and coding techniques, networking protocols, and performance enhancement schemes [11]. Among these aspects, channel modeling constitutes a primary research area due to its critical role in system optimization. Next, we will provide a detailed summary of the research area and problem domain for NLoS UV channels.

When the UV communication range is small and there is an overlap volume between the transmitter (T) beam and the receiver (R) Field-of-View (FoV), single-scattering models [12], [13], [14], [15], [16], [17], [18], [19], [20] can be utilized to investigate the channel characteristics of short-range NLoS UV systems, with distinctions arising from coordinate system choices and transceiver configurations. In [12] and [13], the models were developed based on the prolate-spheroidal coordinate system, which can be used to investigate the angular spectrum of singly scattered energy and the impulse-response duration. Regarding [14], [15], [16], the models were proposed based on the spherical coordinate system, where the model in [15] applies to the case where the sum of the transceiver elevation angles and their half FoV angles is less than 180° and the transceiver FoVs are above the horizontal plane, while the models in [14] and [16] are suitable for the case where transceiver pointing directions can be arbitrary. Concerning [17], [18], [19], [20], they were the simplified versions of the exact single-scattering models [12], [13], [14], [15], [16], which exhibit applicability under constrained geometries. Specifically, the model in [17] applies to the circumstance where the overlap volume between the transmitter beam and the receiver FoV is small, while the models in [18], [19], [20] are suitable for the case where the transmitter beam or receiver FoV is narrow.

As the overlap volume between the transmitter beam and the receiver FoV becomes perceptibly reduced or the communication range increases obviously, multiple-scattering models [21], [22], [23], [24], [25], [26], [27], [28] can be employed to evaluate the channel characteristics of medium-range NLoS UV communication systems. In [21], a channel model was developed based on the Monte-Carlo photon-tracing (MCPT) method, which can be employed to investigate the multiple-scattering impacts of the UV signal and channel bandwidth. Regarding [22], which is an extension of the previous work in [21], it can examine the contributions of different orders of scattering to the resulting estimates of path loss and impulse-response functions (IRFs). Concerning [23], it revealed that the Monte-Carlo integration model adopting the partial importance sampling method has a higher computational efficiency in obtaining IRFs than the MCPT models for higher-order scattering communication scenarios. As regards [24], a multiple-scattering omni-directional model was put forward to analyze the coverage area of NLoS UV communications, while in [25], a theoretical model to acquire the penetration depth of UV radiation in the human skin was studied, which provides guidelines for the power control of UV systems when humans are in the vicinity. Regarding [26], [27], they were the simplified versions of the MCPT model due to its longer simulation time, and consider first- and second-order scattering and second- and third-order scattering, respectively. For [28], a double-scatter semi-analytical channel model for scattering-enhanced NLoS UV scenarios was proposed, where ray-tracing algorithms and nonuniform atmospheric path characterization were integrated to derive low-dimensional integral expressions for single- and double-scatter link gains.

When the communication range exceeds 200 eters, the impact of turbulence effects on the NLoS UV system cannot be neglected [29]. Consequently, studies have been conducted on NLoS UV channel models incorporating atmospheric scattering, absorption, and turbulence effects [30]. Specifically, to improve the accuracy of the channel model for long-range NLoS UV communications, the atmospheric extinction coefficient was modified in [31] based on scintillation attenuation. Besides, a single-scattering turbulent model in a narrow beam case was developed in [32] based on the division of the effective scattering volume, which can examine the turbulence impacts on the probability density functions of the received power in coplanar and noncoplanar situations. In addition, a turbulent channel model adopting the equivalent scattering points approach was put forward in [33] to characterize the fluctuation effect on UV signals with large transceiver FoV angles. Beyond that, the channel properties of single-input multiple-output optical systems were investigated in [34] utilizing photomultiplier tube receivers, which reveals that the statistical combining for maximizing the average signal-to-noise ratio will gradually lose its advantage over the equal-gain combining when the difference among turbulent strengths on all branches diminishes. Apart from those, some empirical path loss models [35], [36] were developed by fitting outdoor measurements, which apply to the cases with fixed transceiver geometries and small communication ranges.

Furthermore, considering the complexity of the NLoS UV communication environment, the aforementioned scattering models cannot accurately evaluate the channel characteristics in scenarios containing obstacles. To address this limitation, studies have been conducted on NLoS UV channel models that incorporate the influence of obstacles. In [37] and [38], two NLoS UV channel models incorporating an obstacle were put forward, where the obstacle's coordinates, thickness, width, height, and orientation angle are considered to approach real-life communication environments. Concerning [39], [40], the MCPT method and integral method were, respectively, employed to model NLoS UV channels containing an obstacle, where the obstacle is regarded as an infinite plane. Regarding [41], the effects of the obstacle on NLoS UV path loss were examined through simulations and experimental measurements, where the thickness of the obstacle is supposed to be infinitely large. In relation to [42], a dynamic offloading framework named FlexSlice was developed, which optimizes the traffic-aware network slicing via a sparse multihead graph attention mechanism for spatio-temporal dependency modeling, and enhances the adaptive resource allocation through a twin delayed deep deterministic policy gradient strategy.

Although these studies lay a solid theoretical foundation for NLoS UV channel modeling, they also face certain challenges

Authorized licensed use limited to: University of Witwatersrand. Downloaded on November 06,2025 at 14:42:10 UTC from IEEE Xplore. Restrictions apply.

with the ongoing complexity of communication environments, as summarized below.

1) Existing NLoS scattering models (e.g., [12], [21], [29]) are not suitable for scenarios with small transceiver elevation angles, because the transmission process of the UV signal is particularly vulnerable to interference from obstacles at such low-angle cases, but these works do not consider obstacles in their modeling.
2) Current obstacle-based models (e.g., [38], [39], [41]) are only applicable to single-obstacle situations and impose constraints on the obstacle shape, namely, cuboid-shaped obstacles. Further, these works assume uniform reflection properties across all the obstacle surfaces. Consequently, they cannot handle scenarios where the reflection surface comprises multiple subregions exhibiting heterogeneous properties.
3) The modeling process of the state-of-the-art work [37] is relatively complicated, which involves various scenarios, cases, conditions, situations, and distance constraints in the derivation process of the scattered energy. This feature poses challenges for generalizing the model to multiple-obstacle scenarios.

To bridge these research gaps, we propose a single-collision model incorporating both air scattering and obstacle reflection effects in this article, which overcomes the challenges faced by the existing NLoS scattering models by considering the impact of obstacles at small elevation angles. In comparison with the existing obstacle-based models, the proposed model accounts for more diverse obstacle shapes, quantities, and more comprehensive reflection properties of obstacle surfaces, thus adapting to more complicated communication environments. Moreover, it demonstrates inherently lower complexity and superior interpretability relative to the state-of-the-art work. For clarity, the main contributions of the article are summarized as follows.

1) First, we investigate the received pulse energy contributed by air scattering, where the typical shapes and numbers of obstacles, as well as their dimensions, orientation angles, and spatial coordinates are incorporated to approach real communication environments. On this basis, an obstacle-boundary approximation method (OBAM) is proposed to reduce the modeling complexity.
2) Then, we derive the received pulse energy obtained from obstacle reflection, where the possible reflection surfaces for different obstacle situations are all incorporated as the obstacle orientation angle changes. Besides, each surface can encompass multiple subregions (i.e., rectangular and circular subregions), and the reflection parameter values of these subregions can be different.
3) Subsequently, the proposed model is verified by comparing it with the MCPT model and the obstacle-free integral model through numerical results. These comparisons reveal that the proposed model exhibits lower channel attenuation than the integral model across all simulated parameters, which is attributed to the dominant contribution of surface reflection in obstructed environments. Further, numerical calculations demonstrate that the proposed OBAM achieves superior performance in estimating path loss for NLoS channels, particularly when dominant obstacle reflection conditions prevail in the propagation environment.

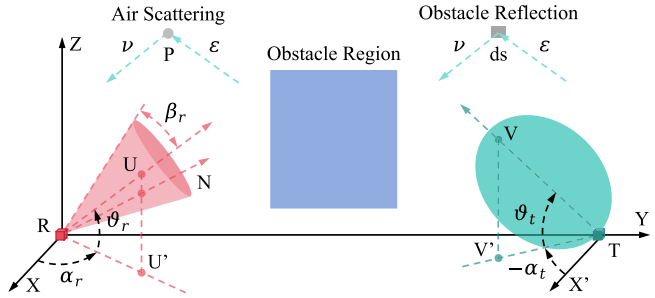


Fig. 1. Diagram of NLoS UV communication scenario considering obstacles.

The remainder of this article is organized as follows. First, the NLoS UV scenarios and relevant model parameter definitions are elaborated in Section II. Second, the received pulse energy contributed by air scattering is investigated in the presence of obstacles in Section III. Beyond that, the received pulse energy contributed by obstacle reflection is investigated in Section VI. Moreover, the proposed single-collision model is examined via simulations in Section V. Finally, the conclusion is presented in Section VI.

Notations: Throughout this article, boldface lowercase letters (e.g., $\boldsymbol{n}$) and boldface uppercase letter pairs (e.g., $\mathbf{RS}$) represent vectors, and $||\cdot||$ denotes the Euclidean norm of a vector.

II. System Model and Parameter Definitions

In the context of real-life IoT environments, the NLoS UV communication scenario can be characterized as depicted in Fig. 1. Given the extensive utilization of the light-emitting diode (LED) in UV communications [43], we select it as the light source and model its radiation intensity distribution as a Lambertian distribution, which is consistent with existing works [44], [45]. Concerning the obstacle region, eight typical obstacle configurations are considered in this article, as shown in Fig. 2, where the typical shapes of the obstacles encompass regular triangular pyramids (RTPYs), regular triangular prisms (RTPs), rectangular prisms (RPs), regular pentagonal prisms (RPPs), and cylinders (CYLs). Further, we consider scenarios where obstacle surfaces comprise multiple subregions, whose contours can be rectangular, circular, or a combination of both, as presented in Fig. 3, consistent with the typical contours of building windows in most cases.

Given the numerous parameters involved in the system model, we systematically categorize them to enhance readability, with representative parameters summarized in Table I. Then, the rigorous definitions for each parameter group are provided for easy understanding.

Transceiver Configurations: As shown in Fig. 1, ϑ_r represents the receiver (R) elevation angle and is positive if taken anticlockwise from RU', where RU' is the projection of the FoV axis RU on the plane XRY; α_r denotes the receiver azimuth angle and is positive if rotating counterclockwise from the X positive axis; ϑ_t denotes the transmitter

Authorized licensed use limited to: University of Witwatersrand. Downloaded on November 06,2025 at 14:42:10 UTC from IEEE Xplore. Restrictions apply.

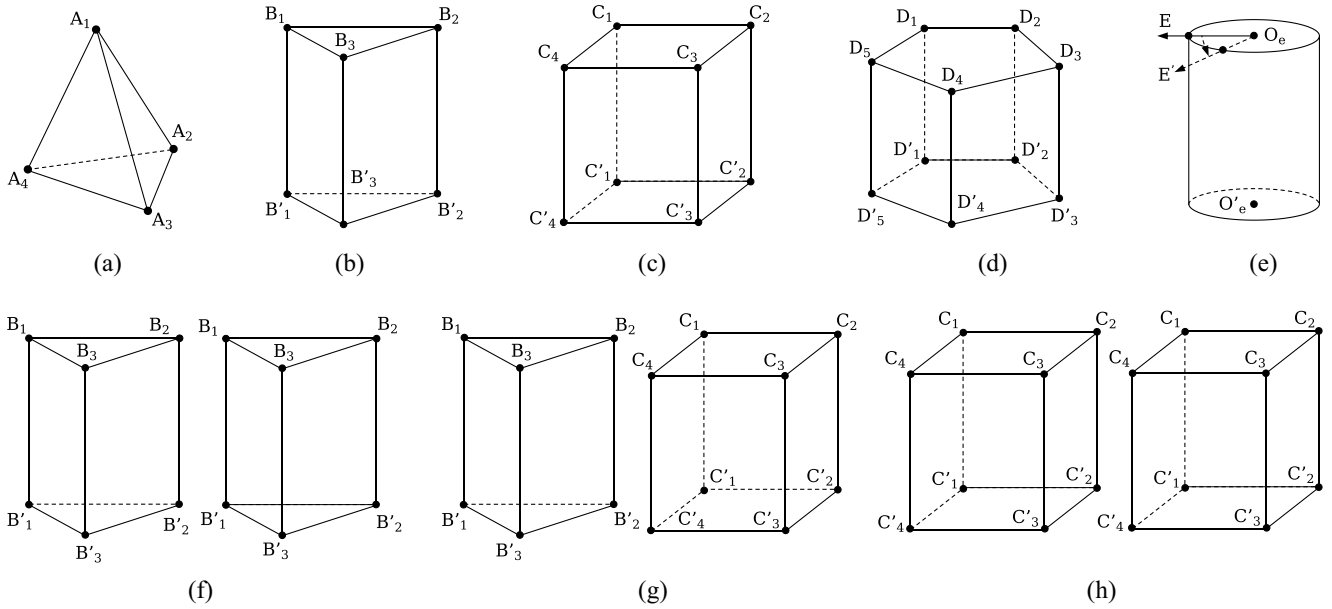


Fig. 2. Shapes and numbers of obstacles appearing in the obstacle region: (a) RTPY. (b) Regular triangular prism. (c) RP. (d) RPP. (e) Cylinder. (f) Two regular triangular prisms. (g) Regular triangular prism and a RP. (h) Two RPs.

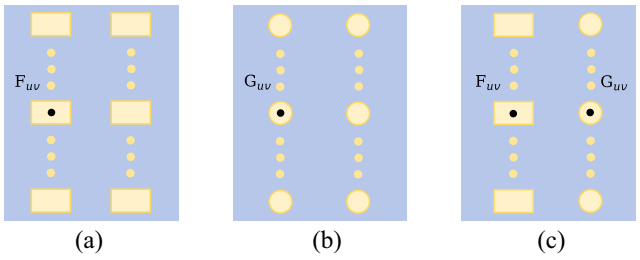


Fig. 3. Obstacle reflection surfaces contain multiple subregions, namely, (a) Rectangles. (b) Circles. (c) Mixture of the two.

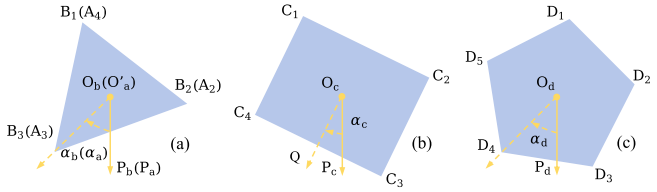


Fig. 4. Illustration of orientation angles for different obstacle shapes, (a) RTP (RTPY). (b) RP. (c) RPP.

(T) elevation angle, which is positive if taken clockwise from the projection of the beam axis TV on the plane XRY; α_t represents the transmitter azimuth angle, which is positive if rotating counterclockwise from TX'; κ represents the order of Lambertian emission; ϖ denotes the angle between the transmitter pointing direction and photon emitting direction; and $\boldsymbol{\mu_r}$ and $\boldsymbol{\mu_t}$ are the unit direction vectors corresponding to the pointing directions of the receiver and transmitter, respectively.

Obstacle Configurations: $\alpha_b(\alpha_a)$ represents the orientation angle of RTP (RTPY), which is positive if rotating clockwise from $\mathbf{O_bP_b}$ ($\mathbf{O'_aP_a}$) to $\mathbf{O_bB_3}$ ($\mathbf{O'_aA_3}$), as shown in Fig. 4; α_c denotes the orientation angle of RP and is positive if taken clockwise from $\mathbf{O_cP_c}$ to $\mathbf{O_cQ}$, where $\mathbf{O_cQ}$ is perpendicular to the line C_3C_4; α_d represents the orientation angle of RPP, which is positive if rotating clockwise from $\mathbf{O_dP_d}$ to $\mathbf{O_dD_4}$; $O_a(x_a, y_a, z_a)$, $O_b(x_b, y_b, z_b)$, $O_c(x_c, y_c, z_c)$, $O_d(x_d, y_d, z_d)$, and $O_e(x_e, y_e, z_e)$ denote the central points of RTPY, RTP, RP, RPP, and CYL, respectively; F_{uv} and G_{uv} represent the central points of the subregions on the obstacle reflection surfaces, and correspond to the rectangular and circular subregions, respectively; w_{uv}, s_{uv}, and r_{uv} are the width and height of the rectangular subregion and the radius of the circular subregion, respectively; $\mathbb{F}_{uv}$ and $\mathbb{G}_{uv}$ represent the reflection regions enclosed by the rectangle and circle, respectively, where u and v denote the subregion $\mathbb{F}_{uv}$ or $\mathbb{G}_{uv}$ is located in the uth column and the vth row; $\Gamma_{\text{rad}}^{\text{sha}}$ denotes the rotation radius of the obstacle, where "sha" can be "RTPY," "RTP," "RP," "RPP," and "CYL"; $(x_{\xi_a}, y_{\xi_a}, z_{\xi_a})$, $(x_{\xi_b}, y_{\xi_b}, z_{\xi_b})$, $(x_{\xi_c}, y_{\xi_c}, z_{\xi_c})$, and $(x_{\xi_d}, y_{\xi_d}, z_{\xi_d})$ represent the coordinates of $\{A_2, A_3, A_4\}$, $\{B_1, B_2, B_3\}$, $\{C_1, C_2, C_3, C_4\}$, and $\{D_1, D_2, D_3, D_4, D_5\}$, respectively, where ξ_a, ξ_b, ξ_c, and ξ_d can be $\{a_2, a_3, a_4\}$, $\{b_1, b_2, b_3\}$, $\{c_1, c_2, c_3, c_4\}$, and $\{d_1, d_2, d_3, d_4, d_5\}$, respectively; v_r denotes the reflection coefficient of the obstacle surface; μ represents the percentage of the incident signal that is reflected diffusely and supposes values between 0 and 1, and m_s is the directivity of the specular components; $\{v_{r,in}, \mu_{in}, m_{s,in}\}$ are the reflection parameter values of $\{v_r, \mu, m_s\}$ in $\mathbb{F}_{uv}$ or $\mathbb{G}_{uv}$, and $\{v_{r,out}, \mu_{out}, m_{s,out}\}$ denote the counterparts outside $\mathbb{F}_{uv}$ or $\mathbb{G}_{uv}$.

Photon Propagation Parameters: ε and ν are the distances from the scattering point P (or the differential reflection area ds) to T and R, respectively; ψ denotes the angle between **RN** and **RS** (**RS** is located on the plane $\mathcal{E}_\vartheta$ and enclosed by the receiver FoV), which is positive when rotating anticlockwise from the ray **RN** as shown in Fig. 1. Here, $\mathcal{E}_\vartheta$ represents the plane passing through RN and is perpendicular to the plane RUU', which rotates around the line RW, where RW

Authorized licensed use limited to: University of Witwatersrand. Downloaded on November 06,2025 at 14:42:10 UTC from IEEE Xplore. Restrictions apply.

TABLE I
CLASSIFICATION OF MODEL PARAMETERS

Type	Parameter	Definition
Transceiver	β_r	The half FoV angle of the receiver
	ϑ_r	The receiver elevation angle
	α_r	The receiver azimuth angle
	$\beta_{1/2}$	The beam's full-width at half-illuminance
	ϑ_t	The transmitter elevation angle
	α_t	The transmitter azimuth angle
	$\mathcal{A}$	The receiver aperture area
	r	The communication range
Obstacle	α_a	The orientation angle of RTPY
	α_b	The orientation angle of RTP
	α_c	The orientation angle of RP
	α_d	The orientation angle of RPP
	ω_a	The length of A_2A_3
	ω_b	The length of B_1B_2
	ω_c	The length of C_1C_2
	μ_c	The length of C_2C_3
	ω_d	The length of D_1D_2
	ω_e	The circle radius of CYL
	γ_a	The height of RTPY
	γ_b	The height of RTP
	γ_c	The height of RP
	γ_d	The height of RPP
	γ_e	The height of CYL
Propagation	ε	The distance from P (or $\mathrm{d}s$) to T
	ν	The distance from P (or $\mathrm{d}s$) to R
	ψ	The angle between **RN** and **RS**
	ϑ	The angle between **RU** and **RN**
	σ	The angle between planes $\mathcal{F}_\sigma$ and LTV'
	β	The angle between **TP** and **PR**
	δ	The angle between **RU** and **RP**
	$\mathcal{S}_{\text{wei}}$	The weighting factor of air scattering
	$\mathcal{R}_{\text{wei}}$	The weighting factor of obstacle reflection
Atmosphere	k_s	The atmospheric scattering coefficient
	$k_{s,ray}$	The Rayleigh scattering coefficient
	$k_{s,mie}$	The Mie scattering coefficient
	k_a	The atmospheric absorption coefficient

is located on the plane XRY and perpendicular to the line RU'. The subscript ϑ denotes the angle between **RU** and **RN**, which is positive if taken anticlockwise from **RU**. Besides, $\mathcal{F}_\sigma$ is defined as the plane that is perpendicular to the plane TVV' and rotates around the line TL, where TL is located on the XRY and perpendicular to the line TV'. The subscript σ denotes the angle between the plane $\mathcal{F}_\sigma$ and the plane LTV', which is positive if rotating clockwise from LTV'. ϑ_i is the incidence angle between the normal vector $\boldsymbol{n}$ of the reflection region and $-\boldsymbol{\varepsilon}$. ϑ_1 and ϑ_2 denote the angles between $\boldsymbol{n}$ and $\boldsymbol{v}$, and $\boldsymbol{v}$ and $\boldsymbol{\varepsilon_s}$, respectively, where $\boldsymbol{\varepsilon_s}$ is the direction vector of the specular reflection of $\boldsymbol{\varepsilon}$, and $\Delta(\vartheta_1, \vartheta_2)$ denotes the reflection pattern of the obstacle surface. Beyond that, $\mathcal{S}_{\text{wei}}$ and $\mathcal{R}_{\text{wei}}$ represent the weighting factors of air scattering and obstacle reflection, respectively, which are utilized to determine whether the scattering point or differential reflection area in the overlap volume of transceiver FoVs is valid or not. If the propagation links of UV photons are not blocked by the obstacle, the values of $\mathcal{S}_{\text{wei}}$ and $\mathcal{R}_{\text{wei}}$ are both equal to 1; otherwise, the counterparts are both equal to 0. Γ_{tmp} denotes the distance from the scattering point P to the central axis of the obstacle, which is adopted to determine whether the coordinates of P lie within the effective rotational regions of the obstacles. If this condition is not satisfied, the scattering point P is deemed invalid. Λ^t_{tmp} and Λ^r_{tmp} represent the horizontal distances from P to the transmitter and receiver, respectively. By imposing constraints on these distances, the effective scattering volume of UV photons can be obtained.

Atmospheric Propagation Parameters: k_e is the extinction coefficient of the atmosphere and can be given by $k_e = k_s + k_a$, where k_s can be expressed as $k_s = k_{s,\text{ray}} + k_{s,\text{mie}}$ [39]. Besides, $\mathcal{P}(\cos\beta)$ denotes the scattering phase function according to [18].

Pulse Energy and Path Loss: $\mathcal{Q}_t$ and $\mathcal{Q}_r$ denote the emitted pulse energy and the received pulse energy, respectively, where $\mathcal{Q}_r$ can be given by $\mathcal{Q}_r = \mathcal{Q}_{r,\text{sca}} + \mathcal{Q}_{r,\text{ref}}$. Here, $\mathcal{Q}_{r,\text{sca}}$ is the received pulse energy contributed by air scattering, and $\mathcal{Q}_{r,\text{ref}}$ is the received pulse energy contributed by obstacle reflection. On this basis, the path loss $\mathcal{L}$ can be defined as

$$\mathcal{L}[\text{dB}] = 10\log_{10}\left[1/\left(\mathcal{Q}_{r,\text{sca}} + \mathcal{Q}_{r,\text{ref}}\right)\right]. \tag{1}$$

Next, we specify the intervals of several variables mentioned above. Considering the symmetries of the obstacles, we set the intervals of α_a, α_b, α_c, and α_d to $[0, 2\pi/3]$, $[0, 2\pi/3]$, $[0, \pi]$, and $[0, 2\pi/5]$, respectively, and set the active areas of points $O_a(x_a, y_a, z_a)$, $O_b(x_b, y_b, z_b)$, $O_c(x_c, y_c, z_c)$, $O_d(x_d, y_d, z_d)$, and $O_e(x_e, y_e, z_e)$ to

$$O_\xi : \begin{cases} x_\xi \in \left(-\infty, -\Gamma^{\text{sha}}_{\text{rad}}\right) \\ y_\xi \in \left(\Gamma^{\text{sha}}_{\text{rad}}, r - \Gamma^{\text{sha}}_{\text{rad}}\right) \\ z_\xi = \gamma_\xi \end{cases} \tag{2}$$

where the subscript ξ can be a, b, c, d, and e. After algebraic operations, $\Gamma^{\text{sha}}_{\text{rad}}$ can be expressed as

$$\Gamma^{\text{sha}}_{\text{rad}} = \begin{cases} \omega_a/\sqrt{3}, & \text{RTPY} \\ \omega_b/\sqrt{3}, & \text{RTP} \\ \sqrt{\omega_c^2 + \mu_c^2}/2, & \text{RP} \\ \omega_d \sin(3\pi/10)/\sin(2\pi/5), & \text{RPP} \\ \omega_e, & \text{CYL.} \end{cases} \tag{3}$$

Thus, the coordinates of the points $\{A_2, A_3, A_4\}$, $\{B_1, B_2, B_3\}$, $\{C_1, C_2, C_3, C_4\}$, and $\{D_1, D_2, D_3, D_4, D_5\}$ can be derived as

$$\begin{cases} x_{\xi_a} = -\Gamma^{\text{RTPY}}_{\text{rad}} \sin(\alpha_a + \varpi_a) + x_a \\ y_{\xi_a} = -\Gamma^{\text{RTPY}}_{\text{rad}} \cos(\alpha_a + \varpi_a) + y_a \\ z_{\xi_a} = 0 \end{cases} \tag{4a}$$

Authorized licensed use limited to: University of Witwatersrand. Downloaded on November 06,2025 at 14:42:10 UTC from IEEE Xplore. Restrictions apply.

$$\begin{cases} x_{\xi_b} = -\Gamma_{\text{rad}}^{\text{RTP}} \sin(\alpha_b + \varpi_b) + x_b \\ y_{\xi_b} = -\Gamma_{\text{rad}}^{\text{RTP}} \cos(\alpha_b + \varpi_b) + y_b \\ z_{\xi_b} = \gamma_b \end{cases} \tag{4b}$$

$$\begin{cases} x_{\xi_c} = -\Gamma_{\text{rad}}^{\text{RP}} \sin(\alpha_c + \varpi_c) + x_c \\ y_{\xi_c} = -\Gamma_{\text{rad}}^{\text{RP}} \cos(\alpha_c + \varpi_c) + y_c \\ z_{\xi_c} = \gamma_c \end{cases} \tag{4c}$$

$$\begin{cases} x_{\xi_d} = -\Gamma_{\text{rad}}^{\text{RPP}} \sin(\alpha_d + \varpi_d) + x_d \\ y_{\xi_d} = -\Gamma_{\text{rad}}^{\text{RPP}} \cos(\alpha_d + \varpi_d) + y_d \\ z_{\xi_d} = \gamma_d \end{cases} \tag{4d}$$

respectively, where the phase $\varpi_a(\varpi_b)$ for the points $A_4(B_1)$, $A_2(B_2)$, and $A_3(B_3)$ are $\pi/6$, $5\pi/6$, and $3\pi/2$, respectively; the phase ϖ_c for C_1, C_2, C_3, and C_4 are $\tan^{-1}(\mu_c/\omega_c)$, $\pi - \tan^{-1}(\mu_c/\omega_c)$, $\pi + \tan^{-1}(\mu_c/\omega_c)$, and $2\pi - \tan^{-1}(\mu_c/\omega_c)$, respectively; and the phase ϖ_d for D_1, D_2, D_3, D_4, and D_5 are $3\pi/10$, $7\pi/10$, $11\pi/10$, $3\pi/2$, and $19\pi/10$, respectively.

Further, we specify the intervals of the transceiver elevation angles, azimuth angles, and the receiver FoV angle. Combining with the active areas of the obstacles, β_r, ϑ_t, and ϑ_r are all set to $(0, \pi/2)$, and α_t and α_r are set to $(-\pi, -\pi/2)$ and $(\pi/2, \pi)$, respectively, which satisfy the commands of general NLoS UV communication scenarios.

Considering the complexity of practical IoT environments, it is necessary to leverage the geospatial mapping platforms (e.g., Google, Apple, and Baidu Maps) for the measurement of obstacle and transceiver configurations during the implementation process. Specifically, with the aid of these platforms, the appropriate placement of transceivers is first selected, and simultaneously, a 3-D Cartesian coordinate system is established by referencing Fig. 1. Subsequently, obstacle parameters, including shapes, dimensions, orientation angles, and coordinates, are measured according to the geospatial mapping platforms. Concurrently, the spatial orientations of all possible reflection surfaces of obstacles are ascertained. Following that, the transceiver elevation angles and azimuth angles are determined based on the obstacle parameters. Notably, the proposed model is designed for static IoT scenarios. Transient obstructions caused by mobile objects can be neglected due to the inherent scattering properties of UV signals.

III. Received Pulse Energy Contributed by Air Scattering

A. Derivation of $\mathcal{Q}_{r,\text{sca}}$

Based on the existing single-scattering propagation theory [37], [43], $\mathcal{Q}_{r,\text{sca}}$ can be derived as

$$\mathcal{Q}_{r,\text{sca}} = \int_{\vartheta_{\min}}^{\vartheta_{\max}} \int_{\psi_{\min}}^{\psi_{\max}} \int_{\nu_{\min}}^{\nu_{\max}} \mathcal{Q}_t k_s \mathcal{A}\, \mathcal{G}\, \mathcal{S}_{\text{wei}}\, \mathrm{d}\nu \mathrm{d}\psi \mathrm{d}\vartheta \tag{5}$$

where

$$\mathcal{G} = \frac{\kappa + 1}{2\pi \varepsilon^2} \cos^{\kappa} \varpi\, \mathcal{P}(\cos\beta) \cos\delta \exp[-k_e(\varepsilon + \nu)] \cos\psi \tag{6a}$$

$$\kappa = -\ln 2 / \ln\cos(\beta_{1/2}/2). \tag{6b}$$

The unknown quantities in (5) are $\vartheta_{\min}$, $\vartheta_{\max}$, $\psi_{\min}$, $\psi_{\max}$, $\nu_{\min}$, $\nu_{\max}$, and $\mathcal{S}_{\text{wei}}$. Given the wide coverage area of the light source based on Lambertian distribution, the upper and lower bounds of the triple integral in $\mathcal{Q}_{r,\text{sca}}$ are mainly determined by the receiver conical surface, and can be derived as

$$\vartheta_{\min} = -\beta_r, \quad \vartheta_{\max} = \beta_r \tag{7}$$

$$\psi_{\max} = \tan^{-1}\left(\frac{\sqrt{\tan^2\beta_r - \tan^2\vartheta}}{\sec\vartheta}\right) = -\psi_{\min} \tag{8}$$

$$\nu_{\min} = 0, \quad \nu_{\max} = +\infty \tag{9}$$

respectively. Meanwhile, a constraint needs to be imposed on the scattering point P, which can be expressed as

$$\frac{1}{\varepsilon} \boldsymbol{\mu_t} \boldsymbol{\varepsilon}^{\mathrm{T}} \geq \cos\frac{\pi}{2}, \text{ i.e.,, } \boldsymbol{\mu_t} \boldsymbol{\varepsilon}^{\mathrm{T}} \geq 0 \tag{10}$$

where $\boldsymbol{\mu_t} = [\cos\vartheta_t \cos\alpha_t, \cos\vartheta_t \sin\alpha_t, \sin\vartheta_t]$ and $\boldsymbol{\varepsilon} = [x, y - r, z]$. Moreover, the coordinates of P can be given by

$$\text{P:} \begin{cases} x = \nu\cos\psi\cos\phi\cos(\alpha_r + \omega)\sec\omega \\ y = \nu\cos\psi\cos\phi\sin(\alpha_r + \omega)\sec\omega \\ z = \nu\cos\psi\sin\phi. \end{cases} \tag{11}$$

Here, $\phi = \vartheta_r + \vartheta$, $\omega = \tan^{-1}(\tan\psi/\cos\phi)$, $\phi_{\min} = \vartheta_r + \vartheta_{\min}$ is assumed to be larger than $-\pi/2$, and $\phi_{\max} = \vartheta_r + \vartheta_{\max}$ is assumed to be less than $\pi/2$. In the following, we will derive the $\mathcal{S}_{\text{wei}}$ values for different obstacle situations.

B. $\mathcal{S}_{wei}$ for Single Obstacle Situations

In this section, we derive the values of $\mathcal{S}_{\text{wei}}$ corresponding to (a) to (e) in Fig. 2 under the condition that the inequality (10) holds. To reduce the modeling complexity, we propose an OBAM to address the boundaries of RTPY, RTP, RP, RPP, and CYL, where the associated obstacle-boundary parameters are defined as follows: $\Upsilon_{r,\text{upp}}^{\text{sha}}$ represents the angle between plane $\mathcal{E}_\vartheta$ and plane WRU' when plane $\mathcal{E}_\vartheta$ is tangent to the top part of the obstacle; $\Upsilon_{r,\max}^{\text{sha}}$ and $\Upsilon_{r,\min}^{\text{sha}}$ denote the maximum and minimum angles, respectively, formed between the rays from point R to the intersection points of plane $\mathcal{E}_\vartheta$ with the obstacle boundary and the reference ray RG, where RG represents the intersection ray between plane $\mathcal{E}_\vartheta$ and plane YRZ; $\Upsilon_{t,\text{upp}}^{\text{sha}}$ is the angle between plane $\mathcal{F}_\sigma$ and plane LTV' when plane $\mathcal{F}_\sigma$ is tangent to the top part of the obstacle; $\Upsilon_{t,\max}^{\text{sha}}$ and $\Upsilon_{t,\min}^{\text{sha}}$ are the maximum and minimum angles, respectively, formed between the rays from point T to the intersection points of plane $\mathcal{F}_\sigma$ with the obstacle boundary and the reference ray TH, where TH represents the intersection ray between plane $\mathcal{F}_\sigma$ and plane YRZ. Based on the geometric relationships, $\Upsilon_{r,\text{upp}}^{\text{sha}}$ and $\Upsilon_{t,\text{upp}}^{\text{sha}}$ can be derived as

$$\Upsilon_{r,\text{upp}}^{\text{sha}} = \begin{cases} \Upsilon_{r,a_1}^{\text{RTPY}} \\ \max\left(\Upsilon_{r,b_1}^{\text{RTP}}, \Upsilon_{r,b_2}^{\text{RTP}}, \Upsilon_{r,b_3}^{\text{RTP}}\right) \\ \max\left(\Upsilon_{r,c_1}^{\text{RP}}, \Upsilon_{r,c_2}^{\text{RP}}, \Upsilon_{r,c_3}^{\text{RP}}, \Upsilon_{r,c_4}^{\text{RP}}\right) \\ \max\left(\Upsilon_{r,d_1}^{\text{RPP}}, \Upsilon_{r,d_2}^{\text{RPP}}, \Upsilon_{r,d_3}^{\text{RPP}}, \Upsilon_{r,d_4}^{\text{RPP}}, \Upsilon_{r,d_5}^{\text{RPP}}\right) \\ \Upsilon_{r,\text{upp}}^{\text{CYL}} \end{cases} \tag{12}$$

$$\Upsilon_{t,\text{upp}}^{\text{sha}} = \begin{cases} \Upsilon_{t,a_1}^{\text{RTPY}} \\ \max\left(\Upsilon_{t,b_1}^{\text{RTP}}, \Upsilon_{t,b_2}^{\text{RTP}}, \Upsilon_{t,b_3}^{\text{RTP}}\right) \\ \max\left(\Upsilon_{t,c_1}^{\text{RP}}, \Upsilon_{t,c_2}^{\text{RP}}, \Upsilon_{t,c_3}^{\text{RP}}, \Upsilon_{t,c_4}^{\text{RP}}\right) \\ \max\left(\Upsilon_{t,d_1}^{\text{RPP}}, \Upsilon_{t,d_2}^{\text{RPP}}, \Upsilon_{t,d_3}^{\text{RPP}}, \Upsilon_{t,d_4}^{\text{RPP}}, \Upsilon_{t,d_5}^{\text{RPP}}\right) \\ \Upsilon_{t,\text{upp}}^{\text{CYL}} \end{cases} \tag{13}$$

Authorized licensed use limited to: University of Witwatersrand. Downloaded on November 06,2025 at 14:42:10 UTC from IEEE Xplore. Restrictions apply.

respectively. Moreover, $\Upsilon_{r,m}^{\text{sha}}$, $\Upsilon_{t,m}^{\text{sha}}$, $\Upsilon_{r,\text{upp}}^{\text{CYL}}$, and $\Upsilon_{t,\text{upp}}^{\text{CYL}}$ can be expressed as

$$\Upsilon_{r,m}^{\text{sha}} = \tan^{-1}\left(\frac{z_m\gamma_r}{|x_m\cot\alpha_r + y_m|}\right) \tag{14}$$

$$\Upsilon_{t,m}^{\text{sha}} = \tan^{-1}\left(\frac{z_m\gamma_t}{|x_m\cot\alpha_t + y_m - r|}\right) \tag{15}$$

$$\Upsilon_{r,\text{upp}}^{\text{CYL}} = \tan^{-1}\left(\frac{\gamma_e\gamma_r}{|x_e\cot\alpha_r + y_e| - \omega_e\gamma_r}\right) \tag{16}$$

$$\Upsilon_{t,\text{upp}}^{\text{CYL}} = \tan^{-1}\left(\frac{\gamma_e\gamma_t}{|x_e\cot\alpha_t + y_e - r| - \omega_e\gamma_t}\right) \tag{17}$$

respectively, where m can be a_1, b_1, b_2, b_3, c_1, c_2, c_3, c_4, d_1, d_2, d_3, d_4, and d_5. Besides, γ_t and γ_r can be given by

$$\gamma_t = \sqrt{\cot^2\alpha_t + 1} \tag{18a}$$

$$\gamma_r = \sqrt{\cot^2\alpha_r + 1}. \tag{18b}$$

Then, $\Upsilon_{r,\max}^{\text{sha}}$ and $\Upsilon_{r,\min}^{\text{sha}}$ can be derived as

$$\Upsilon_{r,\max}^{\text{sha}} = \begin{cases} \max\left(\Upsilon_{r,a_2^1}^{\text{RTPY}}, \Upsilon_{r,a_3^1}^{\text{RTPY}}, \Upsilon_{r,a_4^1}^{\text{RTPY}}\right) \\ \max\left(\Upsilon_{r,b_1^1}^{\text{RTP}}, \Upsilon_{r,b_2^2}^{\text{RTP}}, \Upsilon_{r,b_3^3}^{\text{RTP}}\right) \\ \max\left(\Upsilon_{r,c_1^1}^{\text{RP}}, \Upsilon_{r,c_2^2}^{\text{RP}}, \Upsilon_{r,c_3^3}^{\text{RP}}, \Upsilon_{r,c_4^4}^{\text{RP}}\right) \\ \max\left(\Upsilon_{r,d_1^1}^{\text{RPP}}, \Upsilon_{r,d_2^2}^{\text{RPP}}, \Upsilon_{r,d_3^3}^{\text{RPP}}, \Upsilon_{r,d_4^4}^{\text{RPP}}, \Upsilon_{r,d_5^5}^{\text{RPP}}\right) \\ \max \Upsilon_{r,e_j^i}^{\text{CYL}}, \text{ s. t.}\left(x_{r,e_j^i}, y_{r,e_j^i}, z_{r,e_j^i}\right) \in \mathbb{O}_r \end{cases} \tag{19}$$

$$\Upsilon_{r,\min}^{\text{sha}} = \begin{cases} \min\left(\Upsilon_{r,a_2^1}^{\text{RTPY}}, \Upsilon_{r,a_3^1}^{\text{RTPY}}, \Upsilon_{r,a_4^1}^{\text{RTPY}}\right) \\ \min\left(\Upsilon_{r,b_1^1}^{\text{RTP}}, \Upsilon_{r,b_2^2}^{\text{RTP}}, \Upsilon_{r,b_3^3}^{\text{RTP}}\right) \\ \min\left(\Upsilon_{r,c_1^1}^{\text{RP}}, \Upsilon_{r,c_2^2}^{\text{RP}}, \Upsilon_{r,c_3^3}^{\text{RP}}, \Upsilon_{r,c_4^4}^{\text{RP}}\right) \\ \min\left(\Upsilon_{r,d_1^1}^{\text{RPP}}, \Upsilon_{r,d_2^2}^{\text{RPP}}, \Upsilon_{r,d_3^3}^{\text{RPP}}, \Upsilon_{r,d_4^4}^{\text{RPP}}, \Upsilon_{r,d_5^5}^{\text{RPP}}\right) \\ \min \Upsilon_{r,e_j^i}^{\text{CYL}}, \text{ s. t.}\left(x_{r,e_j^i}, y_{r,e_j^i}, z_{r,e_j^i}\right) \in \mathbb{O}_r \end{cases} \tag{20}$$

respectively, where $\Upsilon_{r,o_j^i}^{\text{sha}}$ denotes the angle between $\mathbf{RP}_{\boldsymbol{r,o_j^i}}$ and $\mathbf{RG}$, and P_{r,o_j^i} represents the intersection point of plane $\mathcal{E}_\vartheta$ with the line O_iO_j or O_iO_i' (e.g., P_{r,a_2^1} and line A_1A_2, or P_{r,b_1^1} and line $\text{B}_1\text{B}_1'$). After algebraic operations, $\Upsilon_{r,o_j^i}^{\text{sha}}$ can be expressed as

$$\Upsilon_{r,o_j^i}^{\text{sha}} = \cos^{-1}\left(\frac{y_{r,o_j^i}\mathcal{G}_3 - z_{r,o_j^i}\mathcal{G}_2}{\sqrt{\mathcal{G}_2^2 + \mathcal{G}_3^2}\left\|\mathbf{RP}_{\boldsymbol{r,o_j^i}}\right\|}\right) \tag{21}$$

where

$$\begin{cases} \mathcal{G}_1 = -\cos\alpha_r\sec^2\vartheta\sin(2\phi)\tan\theta \\ \mathcal{G}_2 = -\sin\alpha_r\sec^2\vartheta\sin(2\phi)\tan\theta \\ \mathcal{G}_3 = 2\sec^2\vartheta\cos^2\phi\tan\theta \end{cases} \tag{22}$$

and θ can be given by $\tan^{-1}(\sec\phi\sqrt{\tan^2\beta_r - \tan^2\vartheta}\cos\vartheta)$.

Regarding RTPY, the coordinates $(x_{r,o_j^i}, y_{r,o_j^i}, z_{r,o_j^i})$ can be derived as

$$\begin{cases} x_{r,o_j^i} = x_{\xi_a} - \dfrac{\mathcal{N}_{\xi_a}^x(\mathcal{G}_1x_{\xi_a} + \mathcal{G}_2y_{\xi_a} + \mathcal{G}_3z_{\xi_a})}{\mathcal{G}_1\mathcal{N}_{\xi_a}^x + \mathcal{G}_2\mathcal{N}_{\xi_a}^y + \mathcal{G}_3\mathcal{N}_{\xi_a}^z} \\ y_{r,o_j^i} = y_{\xi_a} - \dfrac{\mathcal{N}_{\xi_a}^y(\mathcal{G}_1x_{\xi_a} + \mathcal{G}_2y_{\xi_a} + \mathcal{G}_3z_{\xi_a})}{\mathcal{G}_1\mathcal{N}_{\xi_a}^x + \mathcal{G}_2\mathcal{N}_{\xi_a}^y + \mathcal{G}_3\mathcal{N}_{\xi_a}^z} \\ z_{r,o_j^i} = z_{\xi_a} - \dfrac{\mathcal{N}_{\xi_a}^z(\mathcal{G}_1x_{\xi_a} + \mathcal{G}_2y_{\xi_a} + \mathcal{G}_3z_{\xi_a})}{\mathcal{G}_1\mathcal{N}_{\xi_a}^x + \mathcal{G}_2\mathcal{N}_{\xi_a}^y + \mathcal{G}_3\mathcal{N}_{\xi_a}^z} \end{cases} \tag{23}$$

where $[\mathcal{N}_{\xi_a}^x, \mathcal{N}_{\xi_a}^y, \mathcal{N}_{\xi_a}^z] = [x_a - x_{\xi_a}, y_a - y_{\xi_a}, z_a - z_{\xi_a}]$. With respect to RTP, RP, and RPP, $x_{r,o_j^i} = x_{\xi_{b,c,d}}$, $y_{r,o_j^i} = y_{\xi_{b,c,d}}$, and z_{r,o_j^i} can be expressed as

$$z_{r,o_j^i} = -\frac{\mathcal{G}_1x_{r,o_j^i} + \mathcal{G}_2\,y_{r,o_j^i}}{\mathcal{G}_3}. \tag{24}$$

Concerning CYL, $(x_{r,e_j^i}, y_{r,e_j^i}, z_{r,e_j^i})$ represent the coordinates of an arbitrary point within the intersection region $\mathbb{O}_r$ between the plane $\mathcal{E}_\vartheta$ and the cylindrical surface, and $\mathbb{O}_r$ can be defined as

$$\mathbb{O}_r : \begin{cases} \mathcal{G}_1x_{r,e_j^i} + \mathcal{G}_2\,y_{r,e_j^i} + \mathcal{G}_3\,z_{r,e_j^i} = 0 \\ \left(x_{r,e_j^i} - x_e\right)^2 + \left(y_{r,e_j^i} - y_e\right)^2 = \omega_e^2. \end{cases} \tag{25}$$

Following that, $\Upsilon_{t,\max}^{\text{sha}}$ and $\Upsilon_{t,\min}^{\text{sha}}$ can be derived as

$$\Upsilon_{t,\max}^{\text{sha}} = \begin{cases} \max\left(\Upsilon_{t,a_2^1}^{\text{RTPY}}, \Upsilon_{t,a_3^1}^{\text{RTPY}}, \Upsilon_{t,a_4^1}^{\text{RTPY}}\right) \\ \max\left(\Upsilon_{t,b_1^1}^{\text{RTP}}, \Upsilon_{t,b_2^2}^{\text{RTP}}, \Upsilon_{t,b_3^3}^{\text{RTP}}\right) \\ \max\left(\Upsilon_{t,c_1^1}^{\text{RP}}, \Upsilon_{t,c_2^2}^{\text{RP}}, \Upsilon_{t,c_3^3}^{\text{RP}}, \Upsilon_{t,c_4^4}^{\text{RP}}\right) \\ \max\left(\Upsilon_{t,d_1^1}^{\text{RPP}}, \Upsilon_{t,d_2^2}^{\text{RPP}}, \Upsilon_{t,d_3^3}^{\text{RPP}}, \Upsilon_{t,d_4^4}^{\text{RPP}}, \Upsilon_{t,d_5^5}^{\text{RPP}}\right) \\ \max \Upsilon_{t,e_j^i}^{\text{CYL}}, \text{ s. t.}\left(x_{t,e_j^i}, y_{t,e_j^i}, z_{t,e_j^i}\right) \in \mathbb{O}_t \end{cases} \tag{26}$$

$$\Upsilon_{t,\min}^{\text{sha}} = \begin{cases} \min\left(\Upsilon_{t,a_2^1}^{\text{RTPY}}, \Upsilon_{t,a_3^1}^{\text{RTPY}}, \Upsilon_{t,a_4^1}^{\text{RTPY}}\right) \\ \min\left(\Upsilon_{t,b_1^1}^{\text{RTP}}, \Upsilon_{t,b_2^2}^{\text{RTP}}, \Upsilon_{t,b_3^3}^{\text{RTP}}\right) \\ \min\left(\Upsilon_{t,c_1^1}^{\text{RP}}, \Upsilon_{t,c_2^2}^{\text{RP}}, \Upsilon_{t,c_3^3}^{\text{RP}}, \Upsilon_{t,c_4^4}^{\text{RP}}\right) \\ \min\left(\Upsilon_{t,d_1^1}^{\text{RPP}}, \Upsilon_{t,d_2^2}^{\text{RPP}}, \Upsilon_{t,d_3^3}^{\text{RPP}}, \Upsilon_{t,d_4^4}^{\text{RPP}}, \Upsilon_{t,d_5^5}^{\text{RPP}}\right) \\ \min \Upsilon_{t,e_j^i}^{\text{CYL}}, \text{ s. t.}\left(x_{t,e_j^i}, y_{t,e_j^i}, z_{t,e_j^i}\right) \in \mathbb{O}_t \end{cases} \tag{27}$$

respectively, where $\Upsilon_{t,o_j^i}^{\text{sha}}$ denotes the angle between $\mathbf{TP}_{\boldsymbol{t,o_j^i}}$ and $\mathbf{TH}$, and P_{t,o_j^i} represents the intersection point of plane $\mathcal{F}_\sigma$ with the line O_iO_j or O_iO_i' (e.g., P_{t,a_2^1} and line A_1A_2, or P_{t,b_1^1} and line $\text{B}_1\text{B}_1'$). After algebraic operations, $\Upsilon_{t,o_j^i}^{\text{sha}}$ can be given by

$$\Upsilon_{t,o_j^i}^{\text{sha}} = \cos^{-1}\left[\frac{\left(r - y_{t,o_j^i}\right)\cos\sigma - z_{t,o_j^i}\sin\alpha_t\sin\sigma}{\sqrt{\sin^2\alpha_t\sin^2\sigma + \cos^2\sigma}\left\|\mathbf{TP}_{\boldsymbol{t,o_j^i}}\right\|}\right]. \tag{28}$$

Authorized licensed use limited to: University of Witwatersrand. Downloaded on November 06,2025 at 14:42:10 UTC from IEEE Xplore. Restrictions apply.

TABLE II
INTERSECTION CASES BETWEEN THE RECEIVER FOV AND OBSTACLE

$\mathbb{S}_1$	$\Upsilon^{sha}_{r,\max} > \Upsilon^{sha}_{r,\min} \geq \Psi^{r}_{\max} > \Psi^{r}_{\min}$
$\mathbb{S}_2$	$\Upsilon^{sha}_{r,\max} \geq \Psi^{r}_{\max} > \Upsilon^{sha}_{r,\min} > \Psi^{r}_{\min}$
$\mathbb{S}_3$	$\Upsilon^{sha}_{r,\max} \geq \Psi^{r}_{\max} > \Psi^{r}_{\min} \geq \Upsilon^{sha}_{r,\min}$
$\mathbb{S}_4$	$\Psi^{r}_{\max} > \Psi^{r}_{\min} \geq \Upsilon^{sha}_{r,\max} > \Upsilon^{sha}_{r,\min}$
$\mathbb{S}_5$	$\Psi^{r}_{\max} > \Upsilon^{sha}_{r,\max} > \Psi^{r}_{\min} \geq \Upsilon^{sha}_{r,\min}$
$\mathbb{S}_6$	$\Psi^{r}_{\max} > \Upsilon^{sha}_{r,\max} > \Upsilon^{sha}_{r,\min} > \Psi^{r}_{\min}$

Concerning RTPY, the coordinates $(x_{t,o_j^i}, y_{t,o_j^i}, z_{t,o_j^i})$ can be derived as

$$\begin{cases} x_{t,o_j^i} = \mathcal{N}^x_{\xi_a}\zeta + x_{\xi_a} \\ y_{t,o_j^i} = \mathcal{N}^y_{\xi_a}\zeta + y_{\xi_a} \\ z_{t,o_j^i} = \mathcal{N}^z_{\xi_a}\zeta + z_{\xi_a} \end{cases} \tag{29}$$

$$\zeta = \frac{\cos\sigma z_{\xi_a} + \sin\sigma\left[\sin\alpha_t\left(r - y_{\xi_a}\right) - \cos\alpha_t x_{\xi_a}\right]}{\sin\sigma\left(\cos\alpha_t\mathcal{N}^x_{\xi_a} + \sin\alpha_t\mathcal{N}^y_{\xi_a}\right) - \cos\sigma\mathcal{N}^z_{\xi_a}}. \tag{30}$$

Regarding RTP, RP, and RPP, $x_{t,o_j^i} = x_{\xi_{b,c,d}}$, $y_{t,o_j^i} = y_{\xi_{b,c,d}}$, and z_{t,o_j^i} can be expressed as

$$z_{t,o_j^i} = \sin\sigma\cos\alpha_t x_{t,o_j^i} + \sin\sigma\sin\alpha_t\left(y_{t,o_j^i} - r\right)/\cos\sigma. \tag{31}$$

With respect to CYL, $(x_{t,e_j^i}, y_{t,e_j^i}, z_{t,e_j^i})$ denote the coordinates of an arbitrary point within the intersection region $\mathbb{O}_t$ between $\mathcal{F}_\sigma$ and the cylindrical surface, and $\mathbb{O}_t$ can be defined as

$$\mathbb{O}_t: \begin{cases} \left(x_{t,e_j^i} - x_e\right)^2 + \left(y_{t,e_j^i} - y_e\right)^2 = \omega_e^2 \\ \sin\sigma\left[\cos\alpha_t\, x_{t,e_j^i} + \sin\alpha_t\left(y_{t,e_j^i} - r\right)\right] - \cos\sigma\, z_{t,e_j^i} = 0. \end{cases} \tag{32}$$

Moreover, we determine the intersection cases between the receiver FoV and obstacle, which are summarized in Table II. Here, $\Psi^r_{\max}$ and $\Psi^r_{\min}$ represent the maximum and minimum angles, respectively, formed between the rays resulting from the intersection of plane $\mathcal{E}_\vartheta$ with the receiver FoV boundary and the reference ray RG, which can be derived as

$$\Psi^r_{\max} = \alpha_r + \psi_{\max} - \frac{\pi}{2} \tag{33}$$

$$\Psi^r_{\min} = \alpha_r + \psi_{\min} - \frac{\pi}{2}. \tag{34}$$

In summary, the solution process of $\mathcal{S}_{\text{wei}}$ for single obstacle situations can be divided into the following three steps.

Step 1: Judge whether the coordinates (x, y, z) determined by (7), (8), (9), and (11) satisfy inequality (10). If not, assign a value of 0 to $\mathcal{S}_{\text{wei}}$.

Step 2: For the situation where $\phi \geq \Upsilon^{\text{sha}}_{r,\text{upp}}$ and $\sigma \geq \Upsilon^{\text{sha}}_{t,\text{upp}}$, $\mathcal{S}_{\text{wei}} = 1$, where σ can be given by φ, $\pi/2$, and $\pi - \varphi$ for $y + x\cot\alpha_t$ less than r, equal to r, and greater than r, respectively, and φ can be determined through (15). For the situation where $\phi \geq \Upsilon^{\text{sha}}_{r,\text{upp}}$ and $\sigma < \Upsilon^{\text{sha}}_{t,\text{upp}}$, the value of $\mathcal{S}_{\text{wei}}$ equal to 1 has two circumstances: i) Ψ^t_{esp} is less than $\Upsilon^{\text{sha}}_{t,\min}$ or greater than $\Upsilon^{\text{sha}}_{t,\max}$, where Ψ^t_{esp} is the angle between **TP** and **TH**, and ii) $\Lambda^t_{\text{tmp}} < ||\mathbf{TO}'_{\boldsymbol{\xi}}||$, $\Upsilon^{\text{sha}}_{t,\min} \leq \Psi^t_{\text{esp}} \leq \Upsilon^{\text{sha}}_{t,\max}$, and Γ_{tmp} needs to satisfy the following relationship as by

$$\Gamma_{\text{tmp}} > \begin{cases} \Gamma^{\text{sha}}_{\text{rad}}, \text{ RTP, RP, RPP, and CYL} \\ (1 - z/\gamma_a)\,||\boldsymbol{A}'_{\mathbf{1}}\boldsymbol{A}_{\mathbf{2}}||, \text{ RTPY.} \end{cases} \tag{35}$$

For other circumstances in this situation, the value of $\mathcal{S}_{\text{wei}}$ is equal to 0.

Step 3: For the situation where $\phi < \Upsilon^{\text{sha}}_{r,\text{upp}}$, we choose Case $\mathbb{S}_6$ for elaboration because it contains the most comprehensive possibilities compared to Cases $\mathbb{S}_1 \sim \mathbb{S}_5$. If $\Psi^r_{\text{esp}} < \Upsilon^{\text{sha}}_{r,\min}$, the value of $\mathcal{S}_{\text{wei}}$ is equal to 1, where Ψ^r_{esp} is the angle between **RP** and **RG**, while if $\Psi^r_{\text{esp}} \geq \Upsilon^{\text{sha}}_{r,\min}$, the value of $\mathcal{S}_{\text{wei}}$ equal to 1 has two circumstances: i) $\sigma \geq \Upsilon^{\text{sha}}_{t,\text{upp}}$, and ii) $\sigma < \Upsilon^{\text{sha}}_{t,\text{upp}}$ and $\Psi^t_{\text{esp}} < \Upsilon^{\text{sha}}_{t,\min}$. Here, two constraints need to be imposed on the scattering points for $\Upsilon^{\text{sha}}_{r,\min} \leq \Psi^r_{\text{esp}} \leq \Upsilon^{\text{sha}}_{r,\max}$: 1) Γ_{tmp} satisfies the relationship (35), and 2) $\Lambda^r_{\text{tmp}} < ||\mathbf{RO}'_{\boldsymbol{\xi}}||$. For $\Psi^r_{\text{esp}} > \Upsilon^{\text{sha}}_{r,\max}$ and ii) $\sigma < \Upsilon^{\text{sha}}_{t,\text{upp}}$, the situation where $\Psi^t_{\text{esp}} > \Upsilon^{\text{sha}}_{t,\max}$ also needs to be incorporated. For other circumstances in this situation, $\mathcal{S}_{\text{wei}} = 0$.

TABLE III
INTERSECTION CASES AMONG THE RECEIVER FOV AND TWO ARBITRARY OBSTACLES

$\mathbb{D}_1$	$\Upsilon^{sha}_{r,\max} > \Upsilon^{sha}_{r,\min} > \Upsilon^{sha'}_{r,\max} > \Upsilon^{sha'}_{r,\min} \geq \Psi^{r}_{\max} > \Psi^{r}_{\min}$
$\mathbb{D}_2$	$\Upsilon^{sha}_{r,\max} > \Upsilon^{sha}_{r,\min} > \Upsilon^{sha'}_{r,\max} \geq \Psi^{r}_{\max} > \Upsilon^{sha'}_{r,\min} > \Psi^{r}_{\min}$
$\mathbb{D}_3$	$\Upsilon^{sha}_{r,\max} > \Upsilon^{sha}_{r,\min} > \Upsilon^{sha'}_{r,\max} \geq \Psi^{r}_{\max} > \Psi^{r}_{\min} \geq \Upsilon^{sha'}_{r,\min}$
$\mathbb{D}_4$	$\Upsilon^{sha}_{r,\max} > \Upsilon^{sha}_{r,\min} \geq \Psi^{r}_{\max} > \Upsilon^{sha'}_{r,\max} > \Upsilon^{sha'}_{r,\min} > \Psi^{r}_{\min}$
$\mathbb{D}_5$	$\Upsilon^{sha}_{r,\max} > \Upsilon^{sha}_{r,\min} \geq \Psi^{r}_{\max} > \Upsilon^{sha'}_{r,\max} > \Psi^{r}_{\min} \geq \Upsilon^{sha'}_{r,\min}$
$\mathbb{D}_6$	$\Upsilon^{sha}_{r,\max} > \Upsilon^{sha}_{r,\min} \geq \Psi^{r}_{\max} > \Psi^{r}_{\min} \geq \Upsilon^{sha'}_{r,\max} > \Upsilon^{sha'}_{r,\min}$
$\mathbb{D}_7$	$\Upsilon^{sha}_{r,\max} \geq \Psi^{r}_{\max} > \Upsilon^{sha}_{r,\min} > \Upsilon^{sha'}_{r,\max} > \Upsilon^{sha'}_{r,\min} > \Psi^{r}_{\min}$
$\mathbb{D}_8$	$\Upsilon^{sha}_{r,\max} \geq \Psi^{r}_{\max} > \Upsilon^{sha}_{r,\min} > \Upsilon^{sha'}_{r,\max} > \Psi^{r}_{\min} \geq \Upsilon^{sha'}_{r,\min}$
$\mathbb{D}_9$	$\Upsilon^{sha}_{r,\max} \geq \Psi^{r}_{\max} > \Upsilon^{sha}_{r,\min} > \Psi^{r}_{\min} \geq \Upsilon^{sha'}_{r,\max} > \Upsilon^{sha'}_{r,\min}$
$\mathbb{D}_{10}$	$\Upsilon^{sha}_{r,\max} \geq \Psi^{r}_{\max} > \Psi^{r}_{\min} \geq \Upsilon^{sha}_{r,\min} > \Upsilon^{sha'}_{r,\max} > \Upsilon^{sha'}_{r,\min}$
$\mathbb{D}_{11}$	$\Psi^{r}_{\max} > \Upsilon^{sha}_{r,\max} > \Upsilon^{sha}_{r,\min} > \Upsilon^{sha'}_{r,\max} > \Upsilon^{sha'}_{r,\min} > \Psi^{r}_{\min}$
$\mathbb{D}_{12}$	$\Psi^{r}_{\max} > \Upsilon^{sha}_{r,\max} > \Upsilon^{sha}_{r,\min} > \Upsilon^{sha'}_{r,\max} > \Psi^{r}_{\min} \geq \Upsilon^{sha'}_{r,\min}$
$\mathbb{D}_{13}$	$\Psi^{r}_{\max} > \Upsilon^{sha}_{r,\max} > \Upsilon^{sha}_{r,\min} > \Psi^{r}_{\min} \geq \Upsilon^{sha'}_{r,\max} > \Upsilon^{sha'}_{r,\min}$
$\mathbb{D}_{14}$	$\Psi^{r}_{\max} > \Upsilon^{sha}_{r,\max} > \Psi^{r}_{\min} \geq \Upsilon^{sha}_{r,\min} > \Upsilon^{sha'}_{r,\max} > \Upsilon^{sha'}_{r,\min}$
$\mathbb{D}_{15}$	$\Psi^{r}_{\max} > \Psi^{r}_{\min} \geq \Upsilon^{sha}_{r,\max} > \Upsilon^{sha}_{r,\min} > \Upsilon^{sha'}_{r,\max} > \Upsilon^{sha'}_{r,\min}$

C. $\mathcal{S}_{wei}$ for Double Obstacles Situations

In this section, we derive the $\mathcal{S}_{\text{wei}}$ values for the obstacle region containing two obstacles, where the two obstacles can be of the same type as shown in Fig. 2 or of different types, e.g., two RTPs, an RTP and an RP, and two RPs, as shown in Figs. 2 (f), (g), and (h).

Authorized licensed use limited to: University of Witwatersrand. Downloaded on November 06,2025 at 14:42:10 UTC from IEEE Xplore. Restrictions apply.

First, we specify the coordinates of O_ξ and $O_{\xi'}$, which must satisfy the following relationship

$$\left\|\mathbf{O}'_{\boldsymbol{\xi}}\mathbf{O}'_{\boldsymbol{\xi}'}\right\| > \Gamma^{\text{sha}}_{\text{rad}} + \Gamma^{\text{sha}'}_{\text{rad}} \tag{36}$$

where O'_ξ and $O'_{\xi'}$ denote the projections of O_ξ and $O_{\xi'}$ on the plane XRY, respectively, ξ' can be a, b, c, d, or e, and "sha′" can be "RTPY," "RTP," "RP," "RPP," or "CYL." Following that, we investigate the intersection cases among the receiver FoV and two arbitrary obstacles. If ϕ satisfies the following condition:

$$\min\left(\Upsilon^{\text{sha}}_{r,\text{upp}}, \Upsilon^{\text{sha}'}_{r,\text{upp}}\right) \le \phi < \max\left(\Upsilon^{\text{sha}}_{r,\text{upp}}, \Upsilon^{\text{sha}'}_{r,\text{upp}}\right) \tag{37}$$

the plane $\mathcal{E}_\vartheta$ only intersects with one obstacle, and the specific intersection cases are in accordance with Table II, while if $\phi < \min(\Upsilon^{\text{sha}}_{r,\text{upp}}, \Upsilon^{\text{sha}'}_{r,\text{upp}})$, $\mathcal{E}_\vartheta$ intersects with two obstacles, and the intersection cases are summarized in Table III, where $\Upsilon^{\text{sha}}_{r,\min}$ is assumed to be greater than $\Upsilon^{\text{sha}'}_{r,\max}$ and $\Upsilon^{\text{sha}'}_{t,\min}$ is supposed to be greater than $\Upsilon^{\text{sha}}_{t,\max}$ for tractable analysis. Then, the value of $\mathcal{S}_{\text{wei}}$ is investigated under the precondition that inequality (10) holds, which is summarized as following steps.

Step 1: For the situation where $\phi \ge \max(\Upsilon^{\text{sha}}_{r,\text{upp}}, \Upsilon^{\text{sha}'}_{r,\text{upp}})$, we first need to determine the relationship among $\min(\Upsilon^{\text{sha}}_{t,\text{upp}}, \Upsilon^{\text{sha}'}_{t,\text{upp}})$, $\max(\Upsilon^{\text{sha}}_{t,\text{upp}}, \Upsilon^{\text{sha}'}_{t,\text{upp}})$, and σ. Specifically, if $\sigma \ge \max(\Upsilon^{\text{sha}}_{t,\text{upp}}, \Upsilon^{\text{sha}'}_{t,\text{upp}})$, $\mathcal{S}_{\text{wei}} = 1$, while if $\min(\Upsilon^{\text{sha}}_{t,\text{upp}}, \Upsilon^{\text{sha}'}_{t,\text{upp}}) \le \sigma < \max(\Upsilon^{\text{sha}}_{t,\text{upp}}, \Upsilon^{\text{sha}'}_{t,\text{upp}})$, the circumstances for $\mathcal{S}_{\text{wei}}$ equal to 1 are in accordance with those of *Step 2* where $\sigma < \Upsilon^{\text{sha}}_{t,\text{upp}}$ in single obstacle situations. If $\sigma < \min(\Upsilon^{\text{sha}}_{t,\text{upp}}, \Upsilon^{\text{sha}'}_{t,\text{upp}})$, $\mathcal{S}_{\text{wei}} = 1$ has three circumstances: i) Ψ^t_{esp} is less than $\Upsilon^{\text{sha}}_{t,\min}$ or greater than $\Upsilon^{\text{sha}'}_{t,\max}$, or $\Upsilon^{\text{sha}}_{t,\max} < \Psi^t_{\text{esp}} < \Upsilon^{\text{sha}'}_{t,\min}$; ii) $\Lambda^t_{\text{tmp}} < ||\mathbf{TO}'_{\boldsymbol{\xi}}||$ and $\Upsilon^{\text{sha}}_{t,\min} \le \Psi^t_{\text{esp}} \le \Upsilon^{\text{sha}}_{t,\max}$; and iii) $\Lambda^t_{\text{tmp}} < ||\mathbf{TO}'_{\boldsymbol{\xi}'}||$ and $\Upsilon^{\text{sha}'}_{t,\min} \le \Psi^t_{\text{esp}} \le \Upsilon^{\text{sha}'}_{t,\max}$, and the Γ_{tmp} constraints imposed on the scattering points for ii) and iii) must satisfy (35).

Step 2: For the situation where $\min(\Upsilon^{\text{sha}}_{r,\text{upp}}, \Upsilon^{\text{sha}'}_{r,\text{upp}}) \le \phi < \max(\Upsilon^{\text{sha}}_{r,\text{upp}}, \Upsilon^{\text{sha}'}_{r,\text{upp}})$, we choose Case $\mathbb{S}_6$ for elaboration due to its comprehensiveness. If σ is greater than or equal to $\min(\Upsilon^{\text{sha}}_{t,\text{upp}}, \Upsilon^{\text{sha}'}_{t,\text{upp}})$, the derivation of $\mathcal{S}_{\text{wei}}$ is consistent with that of *Step 3* in single obstacle situations. For the scenario where σ is less than $\min(\Upsilon^{\text{sha}}_{t,\text{upp}}, \Upsilon^{\text{sha}'}_{t,\text{upp}})$, the value of $\mathcal{S}_{\text{wei}}$ equal to 1 has three circumstances: i) $\Psi^r_{\text{esp}} < \Upsilon^{\text{sha}}_{r,\min}(\Upsilon^{\text{sha}'}_{r,\min})$; ii) $\Lambda^r_{\text{tmp}} < ||\mathbf{RO}'_{\boldsymbol{\xi}}||(||\mathbf{RO}'_{\boldsymbol{\xi}'}||)$, Γ_{tmp} satisfies (35), and $\Upsilon^{\text{sha}}_{r,\min}(\Upsilon^{\text{sha}'}_{r,\min}) \le \Psi^r_{\text{esp}} \le \Upsilon^{\text{sha}}_{r,\max}(\Upsilon^{\text{sha}'}_{r,\max})$; and iii) $\Psi^r_{\text{esp}} \ge \Upsilon^{\text{sha}}_{r,\max}(\Upsilon^{\text{sha}'}_{r,\max})$, where the settings of Ψ^t_{esp} and Λ^t_{tmp} for ii) and iii) coincide with those of *Step 1* in double obstacle situations where σ is less than $\min(\Upsilon^{\text{sha}}_{t,\text{upp}}, \Upsilon^{\text{sha}'}_{t,\text{upp}})$.

Step 3: For the situation where $\phi < \min(\Upsilon^{\text{sha}}_{r,\text{upp}}, \Upsilon^{\text{sha}'}_{r,\text{upp}})$, we choose Case $\mathbb{D}_{11}$ for elaboration since it contains the most comprehensive possibilities compared to Cases $\mathbb{D}_1 \sim \mathbb{D}_{10}$ and $\mathbb{D}_{12} \sim \mathbb{D}_{15}$. First, we provide the circumstances where $\mathcal{S}_{\text{wei}} = 1$ from the perspective of the receiver: i) Ψ^r_{esp} is less than $\Upsilon^{\text{sha}'}_{r,\min}$ or greater than $\Upsilon^{\text{sha}}_{r,\max}$, or $\Upsilon^{\text{sha}'}_{r,\max} < \Psi^r_{\text{esp}} < \Upsilon^{\text{sha}}_{r,\min}$; ii) $\Upsilon^{\text{sha}'}_{r,\min} \le \Psi^r_{\text{esp}} \le \Upsilon^{\text{sha}'}_{r,\max}$ and $\Lambda^r_{\text{tmp}} < ||\mathbf{RO}'_{\boldsymbol{\xi}'}||$; and iii) $\Upsilon^{\text{sha}}_{r,\min} \le \Psi^r_{\text{esp}} \le \Upsilon^{\text{sha}}_{r,\max}$ and $\Lambda^r_{\text{tmp}} < ||\mathbf{RO}'_{\boldsymbol{\xi}}||$, and the Γ_{tmp} constraints imposed on the scattering points for ii) and iii) need to satisfy the relationship (35). Second, we provide the circumstances of $\mathcal{S}_{\text{wei}}$ equal to 1 from the perspective of the transmitter, which are: (i) $\sigma \ge \max(\Upsilon^{\text{sha}}_{t,\text{upp}}, \Upsilon^{\text{sha}'}_{t,\text{upp}})$; (ii) $\min(\Upsilon^{\text{sha}}_{t,\text{upp}}, \Upsilon^{\text{sha}'}_{t,\text{upp}}) \le \sigma < \max(\Upsilon^{\text{sha}}_{t,\text{upp}}, \Upsilon^{\text{sha}'}_{t,\text{upp}})$, where the settings of Ψ^t_{esp}, Λ^t_{tmp}, and Γ_{tmp} are in accordance with those of *Step 2* in single obstacle situations where $\sigma < \Upsilon^{\text{sha}}_{t,\text{upp}}$; and (iii) $\sigma < \min(\Upsilon^{\text{sha}}_{t,\text{upp}}, \Upsilon^{\text{sha}'}_{t,\text{upp}})$ and the settings of Ψ^t_{esp}, Λ^t_{tmp}, and Γ_{tmp} are in accordance with those of *Step 1* in double obstacle situations. If the coordinates of the scattering point satisfies the aforementioned circumstances from the perspectives of both the transmitter and receiver, $\mathcal{S}_{\text{wei}} = 1$; otherwise, $\mathcal{S}_{\text{wei}} = 0$.

D. $\mathcal{S}_{wei}$ for Multiple Obstacles Situations

In this section, we also provide the solution steps of $\mathcal{S}_{\text{wei}}$ for the obstacle region containing multiple obstacles, where the shapes of the obstacles can be of the same type or different types. Initially, the coordinates and dimensions of the obstacles need to be specified, which must satisfy the precondition that the distance between the central points of any two obstacles is longer than the sum of their rotation radii. Following that, the intersection cases among $\mathcal{E}_\vartheta$ and multiple obstacles need to be analyzed for different ϕ values, where the ϕ interval is divided into multiple subintervals by the $\Upsilon^{\text{sha}}_{r,\text{upp}}$ value corresponding to multiple obstacles. Moreover, the intersection cases among $\mathcal{F}_\sigma$ and multiple obstacles need to be investigated, where the σ interval is divided into multiple subintervals by the $\Upsilon^{\text{sha}}_{t,\text{upp}}$ value corresponding to multiple obstacles. Finally, we analyze the circumstances where $\mathcal{S}_{\text{wei}} = 1$ from the perspectives of both the transmitter and receiver.

In contrast to the latest research [37], which applies an exact treatment to the obstacle boundary, the proposed model adopts an approximate treatment to the obstacle boundaries, resulting in a markedly lower complexity for solving $\mathcal{S}_{\text{wei}}$ than that of research [37]. Moreover, this advantage will become more prominent as the number of obstacles increases.

For the proposed OBAM, its performance is closely related to the difference between the obstacle volume and its rotational volume. Specifically, when the reflectivity of the obstacle surface is relatively high, OBAM performance is generally distinguished, and the influence of the difference between the obstacle volume and its rotational volume becomes negligible. However, under conditions of low obstacle surface reflectivity, OBAM performance is relatively good when the difference between the obstacle volume and its rotational volume is less significant. Conversely, when this difference is large, OBAM performance will become relatively poor.

IV. Received Pulse Energy Contributed by Obstacle Reflection

A. Derivation of $\mathcal{Q}_{r,ref}$

Based on the existing UV reflection propagation theory [37], [40], [46], $\mathcal{Q}_{r,\text{ref}}$ can be derived as

$$\mathcal{Q}_{r,\text{ref}} = \iint_{\mathcal{S}} \frac{\mathcal{Q}_t(\kappa+1)\cos^\kappa \varpi \cos\vartheta_i \cos\delta}{2\pi\varepsilon^2\nu^2} \times \mathcal{A}\, v_r\, \Delta(\vartheta_1, \vartheta_2) \exp[-k_e(\varepsilon+\nu)]\, \mathcal{R}_{\text{wei}}\, \mathrm{d}s \tag{38}$$

Authorized licensed use limited to: University of Witwatersrand. Downloaded on November 06,2025 at 14:42:10 UTC from IEEE Xplore. Restrictions apply.

where

$$\Delta(\vartheta_1, \vartheta_2) = \mu \frac{\cos \vartheta_1}{\pi} + (1-\mu)\frac{m_s+1}{2\pi}\cos^{m_s}\vartheta_2. \quad (39)$$

Next, we will determine the effective reflection regions $\mathcal{S}$, ds, and $\mathcal{R}_{\text{wei}}$ combined with the specific obstacle situations.

B. Effective Reflection Regions Without SubRegions

In this part, the effective reflection regions for the obstacles RTPY, RTP, RP, RPP, and CYL are investigated under the precondition that the reflection parameter values for all points on the same surface are identical. According to the geometric relationships, the effective reflection regions for RTPY can be expressed as

$$\mathcal{S}_{\text{RTPY}}: \begin{cases} x \in \left(-\Gamma_{\text{rad}}^{\text{RTPY}} + x_a, \Gamma_{\text{rad}}^{\text{RTPY}} + x_a\right) \\ y \in \left(-\Gamma_{\text{rad}}^{\text{RTPY}} + y_a, \Gamma_{\text{rad}}^{\text{RTPY}} + y_a\right) \\ \boldsymbol{n}_{\boldsymbol{\xi_a}}\left[x - x_a,\, y - y_a,\, z - z_a\right]^{\text{T}} = 0 \\ \Theta_\rho, \Theta_{\rho'} \in \left[0, 2\pi/3\right],\ \Theta_\rho + \Theta_{\rho'} = 2\pi/3 \\ \left\|\mathbf{O}_{\boldsymbol{a}}'\mathbf{P}'\right\| \le \left\|\mathbf{O}_{\boldsymbol{a}}'\mathbf{P}_{\text{thr}}\right\| \\ \boldsymbol{\mu_t}\,\boldsymbol{\varepsilon}^{\text{T}} \ge 0,\ \boldsymbol{\mu_r}\,(-\boldsymbol{\nu})^{\text{T}} \ge \nu\cos\beta_r \end{cases} \quad (40)$$

where $(\cdot)^{\text{T}}$ denotes the matrix transpose operator, and $\boldsymbol{n}_{\boldsymbol{\xi_a}} = [n_{\xi_a}^x, n_{\xi_a}^y, n_{\xi_a}^z]$ is the normal vector of the surfaces $A_1A_4A_3$ where $(\xi_a, \xi_a') = (a_4, a_3)$, $A_1A_3A_2$ where $(\xi_a, \xi_a') = (a_3, a_2)$, and $A_1A_2A_4$ where $(\xi_a, \xi_a') = (a_2, a_4)$, and can be given by

$$n_{\xi_a}^x = \left[y_{\xi_a} - y_a,\, z_{\xi_a} - z_a\right]\left[z_{\xi_a'} - z_a,\, y_a - y_{\xi_a'}\right]^{\text{T}} \quad (41a)$$

$$n_{\xi_a}^y = \left[z_{\xi_a} - z_a,\, x_{\xi_a} - x_a\right]\left[x_{\xi_a'} - x_a,\, z_a - z_{\xi_a'}\right]^{\text{T}} \quad (41b)$$

$$n_{\xi_a}^z = \left[x_{\xi_a} - x_a,\, y_{\xi_a} - y_a\right]\left[y_{\xi_a'} - y_a,\, x_a - x_{\xi_a'}\right]^{\text{T}}. \quad (41c)$$

Regarding Θ_ρ and $\Theta_{\rho'}$, they denote the angles between $\mathbf{O}_{\boldsymbol{a}}'\mathbf{P}'$ and $\mathbf{O}_{\boldsymbol{a}}'\mathbf{A}_{\boldsymbol{\rho}}$, and $\mathbf{O}_{\boldsymbol{a}}'\mathbf{P}'$ and $\mathbf{O}_{\boldsymbol{a}}'\mathbf{A}_{\boldsymbol{\rho'}}$, respectively, where (ρ, ρ') can be $(4, 3)$, $(3, 2)$, and $(2, 4)$, and P$'$ is the projection point of P onto the plane XRY. Concerning the point P_{thr}, which is the intersection point between the lines $O_a'\text{P}'$ and $\text{A}_\rho\text{A}_{\rho'}$, its coordinates can be derived as

$$x_{\text{thr}} = \frac{y_{\text{thr}} - y_a}{k_x} + x_a \quad (42a)$$

$$y_{\text{thr}} = \frac{k_{\xi_a}(k_x x_a - y_a) + k_x\left(y_{\xi_a'} - x_{\xi_a'}k_{\xi_a}\right)}{k_x - k_{\xi_a}} \quad (42b)$$

where $k_x = (y - y_a)/(x - x_a)$ and $k_{\xi_a} = (y_{\xi_a} - y_{\xi_a'})/(x_{\xi_a} - x_{\xi_a'})$. Note that for the case where $x_{\text{thr}} = x_a$, $y_{\text{thr}} = y_{\xi_a'} + k_{\xi_a}(x_{\text{thr}} - x_{\xi_a'})$, while for the case where $y_{\text{thr}} = y_a$, $x_{\text{thr}} = x_{\xi_a'} + (y_{\text{thr}} - y_{\xi_a'})/k_{\xi_a}$, and for the case where $x_{\xi_a} = x_{\xi_a'}$, $x_{\text{thr}} = x_{\xi_a}$ and $y_{\text{thr}} = y_a + k_x(x_{\text{thr}} - x_a)$. As for the case where $y_{\xi_a} = y_{\xi_a'}$, $y_{\text{thr}} = y_{\xi_a}$, and $x_{\text{thr}} = x_a + (y_{\text{thr}} - y_a)/\,k_x$. Besides, $\boldsymbol{\mu_r}$ can be expressed as $[\cos\vartheta_r\cos\alpha_r, \cos\vartheta_r\sin\alpha_r, \sin\vartheta_r]$. Thus, d$s$ can be derived as

$$\text{d}s = \sqrt{1 + \left(\frac{n_{\xi_a}^x}{n_{\xi_a}^z}\right)^2 + \left(\frac{n_{\xi_a}^y}{n_{\xi_a}^z}\right)^2}\,\text{d}x\text{d}y. \quad (43)$$

Combined with the geometries of RTP, RP, and RPP, they all have three potential reflection surfaces, which can be expressed as

$$\mathcal{S}_{\text{RTP}}: \begin{cases} y \in \left[y_{b_1}, y_{b_3}\right], & \text{surface } \text{B}_{133'1'} \\ y \in \left[y_{b_3}, y_{b_2}\right], & \text{surface } \text{B}_{322'3'} \\ y \in \left[y_{b_2}, y_{b_1}\right], & \text{surface } \text{B}_{211'2'} \\ x = k_{b_{13}} + x_{b_3}, & \text{surface } \text{B}_{133'1'} \\ x = k_{b_{32}} + x_{b_2}, & \text{surface } \text{B}_{322'3'} \\ x = k_{b_{21}} + x_{b_1}, & \text{surface } \text{B}_{211'2'} \\ z \in \left[0, \gamma_b\right] \end{cases} \quad (44)$$

$$\mathcal{S}_{\text{RP}}: \begin{cases} y \in \left[y_{c_4}, y_{c_3}\right], & \text{surface } \text{C}_{433'4'} \\ y \in \left[y_{c_3}, y_{c_2}\right], & \text{surface } \text{C}_{322'3'} \\ y \in \left[y_{c_2}, y_{c_1}\right], & \text{surface } \text{C}_{211'2'} \\ x = k_{c_{43}} + x_{c_3}, & \text{surface } \text{C}_{433'4'} \\ x = k_{c_{32}} + x_{c_2}, & \text{surface } \text{C}_{322'3'} \\ x = k_{c_{21}} + x_{c_1}, & \text{surface } \text{C}_{211'2'} \\ z \in \left[0, \gamma_c\right] \end{cases} \quad (45)$$

$$\mathcal{S}_{\text{RPP}}: \begin{cases} y \in \left[y_{d_5}, y_{d_4}\right], & \text{surface } \text{D}_{544'5'} \\ y \in \left[y_{d_4}, y_{d_3}\right], & \text{surface } \text{D}_{433'4'} \\ y \in \left[y_{d_3}, y_{d_2}\right], & \text{surface } \text{D}_{322'3'} \\ x = k_{d_{54}} + x_{d_4}, & \text{surface } \text{D}_{544'5'} \\ x = k_{d_{43}} + x_{d_3}, & \text{surface } \text{D}_{433'4'} \\ x = k_{d_{32}} + x_{d_2}, & \text{surface } \text{D}_{322'3'} \\ z \in \left[0, \gamma_d\right] \end{cases} \quad (46)$$

respectively, where $\text{B}_{133'1'}$ represents the surface $\text{B}_1\text{B}_3\text{B}_3'\text{B}_1'$, and is also suitable for the remaining expressions. When these surfaces are valid, the corresponding α_b, α_c, and α_d intervals are given by

$$\mathcal{S}_{\text{RTP}}: \begin{cases} \alpha_b \in [0, \pi/6), & \textit{surface } B_{133'1'} \\ \alpha_b \in [0, 2\pi/3], & \textit{surface } B_{322'3'} \\ \alpha_b \in (\pi/2, 2\pi/3], & \text{surface } \text{B}_{211'2'} \end{cases} \quad (47)$$

$$\mathcal{S}_{\text{RP}}: \begin{cases} \alpha_c \in \left[0, \pi/2\right), & \text{surface } \text{C}_{433'4'} \\ \alpha_c \in (0, \pi), & \text{surface } \text{C}_{322'3'} \\ \alpha_c \in (\pi/2, \pi], & \text{surface } \text{C}_{211'2'} \end{cases} \quad (48)$$

$$\mathcal{S}_{\text{RPP}}: \begin{cases} \alpha_d \in \left[0, 3\pi/10\right), & \text{surface } \text{D}_{544'5'} \\ \alpha_d \in [0, 2\pi/5], & \text{surface } \text{D}_{433'4'} \\ \alpha_d \in (\pi/10, 2\pi/5], & \text{surface } \text{D}_{322'3'} \end{cases} \quad (49)$$

respectively. On these bases, $k_{\varrho ij}$ can be derived as

$$k_{\varrho ij} = \frac{(x_{\varrho_i} - x_{\varrho_j})(y - y_{\varrho_j})}{y_{\varrho_i} - y_{\varrho_j}} \quad (50)$$

where ϱ can be b, c, and d, and meanwhile, the corresponding normal vector of these surfaces can be given by

$$\boldsymbol{n}_{\boldsymbol{\xi_\varrho}} = \left[\gamma_\varrho(y_{\varrho_j} - y_{\varrho_i}), \gamma_\varrho(x_{\varrho_i} - x_{\varrho_j}), 0\right]. \quad (51)$$

Further, the coordinates (x, y, z) must satisfy the relationships that $\boldsymbol{\mu_t}\boldsymbol{\varepsilon}^{\text{T}} \ge 0$ and $\boldsymbol{\mu_r}(-\boldsymbol{\nu})^{\text{T}} \ge \nu\cos\beta_r$, and the expressions

Authorized licensed use limited to: University of Witwatersrand. Downloaded on November 06,2025 at 14:42:10 UTC from IEEE Xplore. Restrictions apply.

of ds can be derived as

$$\mathrm{d}s = \begin{cases} \frac{\mathrm{d}y\mathrm{d}z}{\sin(\pi/6-\alpha_b)}, & \text{surface } \mathrm{B}_{133'1'} \\ \frac{\mathrm{d}y\mathrm{d}z}{\sin(\pi/6+\alpha_b)}, & \text{surface } \mathrm{B}_{322'3'} \\ \frac{\mathrm{d}y\mathrm{d}z}{\sin(\alpha_b-\pi/2)}, & \text{surface } \mathrm{B}_{211'2'} \\ \frac{\mathrm{d}y\mathrm{d}z}{\cos\alpha_c}, & \text{surface } \mathrm{C}_{433'4'} \\ \frac{\mathrm{d}y\mathrm{d}z}{\sin\alpha_c}, & \text{surface } \mathrm{C}_{322'3'} \\ \frac{\mathrm{d}y\mathrm{d}z}{-\cos\alpha_c}, & \text{surface } \mathrm{C}_{211'2'} \\ \frac{\mathrm{d}y\mathrm{d}z}{\sin(3\pi/10-\alpha_d)}, & \text{surface } \mathrm{D}_{544'5'} \\ \frac{\mathrm{d}y\mathrm{d}z}{\cos(\alpha_d-\pi/5)}, & \text{surface } \mathrm{D}_{433'4'} \\ \frac{\mathrm{d}y\mathrm{d}z}{\sin(\alpha_d-\pi/10)}, & \text{surface } \mathrm{D}_{322'3'}. \end{cases} \tag{52}$$

Beyond that, the effective reflection region for CYL can be expressed as

$$\mathcal{S}_{\mathrm{CYL}}: \begin{cases} \Phi \in (0, \pi) \\ \boldsymbol{\mu_t}\boldsymbol{\varepsilon}^{\mathrm{T}} \geq \varepsilon\cos(\pi/2) \\ \boldsymbol{\mu_r}(-\boldsymbol{\nu})^{\mathrm{T}} \geq \nu\cos\beta_r \\ (x-x_e)^2+(y-y_e)^2=\omega_e^2 \\ x = x_e + \omega_e\sin\Phi \\ y = y_e - \omega_e\cos\Phi \\ z \in [0, \gamma_e] \end{cases} \tag{53}$$

where Φ represents the angle between $\mathbf{O_eE}$ and $\mathbf{O_eE'}$, which is positive if taken counterclockwise from $\mathbf{O_eE}$, and ds can be expressed as $\omega_e\mathrm{d}\Phi\mathrm{d}z$.

C. Effective Reflection Regions With SubRegions

Then, we determine the effective reflection regions for the obstacle surface encompassing multiple subregions, as shown in Fig. 3, where the shape of the obstacle side is assumed to be rectangular, which is consistent with the shape of the sides of most buildings in real-life environments. Throughout the entire modeling process, the contours of the subregions are modeled as 1) rectangles; 2) circles; or 3) a mixture of the two. Thus, the relevant effective reflection regions can be derived as

$$\begin{cases} z \in [0, \gamma_{\varrho}], & sha \\ y \in [y_{\varrho i}, y_{\varrho j}], & \text{surface } \mathbb{W}_{ijj'i'} \\ x = k_{\varrho ij} + x_{\varrho j}, & \text{surface } \mathbb{W}_{ijj'i'} \\ (x,y,z) \in \mathbb{F}_{uv} \text{ or } \mathbb{G}_{uv}, & \{v_{r,in}, \mu_{in}, m_{s,in}\} \\ (x,y,z) \notin \mathbb{F}_{uv} \text{ or } \mathbb{G}_{uv}, & \{v_{r,out}, \mu_{out}, m_{s,out}\} \end{cases} \tag{54}$$

where $\mathbb{W}$ can be B, C, or D, and the value combinations of i and j are in accordance with those in (44)–(46). Furthermore, $\mathbb{F}_{uv}$ and $\mathbb{G}_{uv}$ can be expressed as

$$\mathbb{F}_{uv}: \begin{cases} z \in \left[z_{uv} - \frac{1}{2}s_{uv}, z_{uv} + \frac{1}{2}s_{uv}\right] \\ y \in \left[y_{uv} - \frac{\mathrm{d}y\mathrm{d}z}{2\,\mathrm{d}s}w_{uv}, y_{uv} + \frac{\mathrm{d}y\mathrm{d}z}{2\,\mathrm{d}s}w_{uv}\right] \end{cases} \tag{55}$$

$$\mathbb{G}_{uv}: (x-x_{uv})^2+(y-y_{uv})^2+(z-z_{uv})^2 \leq r_{uv}^2. \tag{56}$$

D. $\mathcal{R}_{wei}$ for Different Obstacle Situations

Next, we investigate the value of $\mathcal{R}_{\mathrm{wei}}$. For single obstacle situations, $\mathcal{Q}_{r,\mathrm{ref}}$ is contributed by one obstacle, and the value of $\mathcal{R}_{\mathrm{wei}}$ is always equal to 1. As for double obstacle situations, $\mathcal{Q}_{r,\mathrm{ref}}$ is contributed by two obstacles, and the value of $\mathcal{R}_{\mathrm{wei}}$ is closely related to the relative positions of the two obstacles. For easy understanding, we first investigate the circumstances where $\mathcal{R}_{\mathrm{wei}}=1$ from the perspective of the receiver. Because of the similarity, we assume that $\Upsilon_{r,\max}^{\mathrm{sha}}$ is greater than $\Upsilon_{r,\max}^{\mathrm{sha}'}$, and meanwhile discuss the relationship among $\Upsilon_{r,\min}^{\mathrm{sha}}$, $\Upsilon_{r,\max}^{\mathrm{sha}'}$, and $\Upsilon_{r,\min}^{\mathrm{sha}'}$, which are summarized as: i) $\Upsilon_{r,\min}^{\mathrm{sha}} \geq \Upsilon_{r,\max}^{\mathrm{sha}'}$; ii) $\Upsilon_{r,\max}^{\mathrm{sha}'} > \Upsilon_{r,\min}^{\mathrm{sha}} \geq \Upsilon_{r,\min}^{\mathrm{sha}'}$; and iii) $\Upsilon_{r,\min}^{\mathrm{sha}'} > \Upsilon_{r,\min}^{\mathrm{sha}}$. In case i), $\mathcal{R}_{\mathrm{wei}}=1$. In case ii), if $x_\xi + \Gamma_{\mathrm{rad}}^{\mathrm{sha}} \geq x_{\xi'} + \Gamma_{\mathrm{rad}}^{\mathrm{sha}'}$, $\mathcal{R}_{\mathrm{wei}}=1$ when $\Psi_{\mathrm{esp}}^r \in [\Upsilon_{r,\min}^{\mathrm{sha}'}, \Upsilon_{r,\min}^{\mathrm{sha}}]^{\mathrm{sha}'} \cup (\Upsilon_{r,\min}^{\mathrm{sha}}, \Upsilon_{r,\max}^{\mathrm{sha}}]^{\mathrm{sha}}$, and if $x_\xi + \Gamma_{\mathrm{rad}}^{\mathrm{sha}} < x_{\xi'} + \Gamma_{\mathrm{rad}}^{\mathrm{sha}'}$, $\mathcal{R}_{\mathrm{wei}}=1$ when $\Psi_{\mathrm{esp}}^r \in [\Upsilon_{r,\min}^{\mathrm{sha}'}, \Upsilon_{r,\max}^{\mathrm{sha}'}]^{\mathrm{sha}'} \cup (\Upsilon_{r,\max}^{\mathrm{sha}'}, \Upsilon_{r,\max}^{\mathrm{sha}}]^{\mathrm{sha}}$, where the superscripts sha and sha$'$ apply to distinguish different obstacles. In case iii), if $x_\xi + \Gamma_{\mathrm{rad}}^{\mathrm{sha}} > x_{\xi'} + \Gamma_{\mathrm{rad}}^{\mathrm{sha}'}$, $\mathcal{R}_{\mathrm{wei}}=1$ when $\Psi_{\mathrm{esp}}^r \in [\Upsilon_{r,\min}^{\mathrm{sha}}, \Upsilon_{r,\max}^{\mathrm{sha}}]^{\mathrm{sha}}$, while if $x_\xi + \Gamma_{\mathrm{rad}}^{\mathrm{sha}} \leq x_{\xi'} + \Gamma_{\mathrm{rad}}^{\mathrm{sha}'}$, $\mathcal{R}_{\mathrm{wei}}=1$ when $\Psi_{\mathrm{esp}}^r \in [\Upsilon_{r,\min}^{\mathrm{sha}}, \Upsilon_{r,\min}^{\mathrm{sha}'}]^{\mathrm{sha}} \cup (\Upsilon_{r,\min}^{\mathrm{sha}'}, \Upsilon_{r,\max}^{\mathrm{sha}'})^{\mathrm{sha}'} \cup [\Upsilon_{r,\max}^{\mathrm{sha}'}, \Upsilon_{r,\max}^{\mathrm{sha}}]^{\mathrm{sha}}$.

Moreover, we investigate the circumstances where $\mathcal{R}_{\mathrm{wei}}=1$ from the perspective of the transmitter. Due to the similarity, we suppose that $\Upsilon_{t,\max}^{\mathrm{sha}'}$ is greater than $\Upsilon_{t,\max}^{\mathrm{sha}}$, and at the same time discuss the relationship among $\Upsilon_{t,\min}^{\mathrm{sha}'}$, $\Upsilon_{t,\max}^{\mathrm{sha}}$, and $\Upsilon_{t,\min}^{\mathrm{sha}}$, which are summarized as: (i) $\Upsilon_{t,\min}^{\mathrm{sha}'} \geq \Upsilon_{t,\max}^{\mathrm{sha}}$; (ii) $\Upsilon_{t,\max}^{\mathrm{sha}} > \Upsilon_{t,\min}^{\mathrm{sha}'} \geq \Upsilon_{t,\min}^{\mathrm{sha}}$; and (iii) $\Upsilon_{t,\min}^{\mathrm{sha}} > \Upsilon_{t,\min}^{\mathrm{sha}'}$. In case (i), $\mathcal{R}_{\mathrm{wei}}$ is always equal to 1. In case (ii), if $x_{\xi'} + \Gamma_{\mathrm{rad}}^{\mathrm{sha}'} \geq x_\xi + \Gamma_{\mathrm{rad}}^{\mathrm{sha}}$, $\mathcal{R}_{\mathrm{wei}}=1$ when $\Psi_{\mathrm{esp}}^t \in [\Upsilon_{t,\min}^{\mathrm{sha}}, \Upsilon_{t,\min}^{\mathrm{sha}'}]^{\mathrm{sha}} \cup (\Upsilon_{t,\min}^{\mathrm{sha}'}, \Upsilon_{t,\max}^{\mathrm{sha}'}]^{\mathrm{sha}'}$, while if $x_{\xi'} + \Gamma_{\mathrm{rad}}^{\mathrm{sha}'} < x_\xi + \Gamma_{\mathrm{rad}}^{\mathrm{sha}}$, $\mathcal{R}_{\mathrm{wei}}=1$ when $\Psi_{\mathrm{esp}}^t \in [\Upsilon_{t,\min}^{\mathrm{sha}}, \Upsilon_{t,\max}^{\mathrm{sha}}]^{\mathrm{sha}} \cup (\Upsilon_{t,\max}^{\mathrm{sha}}, \Upsilon_{t,\max}^{\mathrm{sha}'}]^{\mathrm{sha}'}$. Regarding case (iii), if $x_{\xi'} + \Gamma_{\mathrm{rad}}^{\mathrm{sha}'} > x_\xi + \Gamma_{\mathrm{rad}}^{\mathrm{sha}}$, $\mathcal{R}_{\mathrm{wei}}=1$ when $\Psi_{\mathrm{esp}}^t \in [\Upsilon_{t,\min}^{\mathrm{sha}'}, \Upsilon_{t,\max}^{\mathrm{sha}'}]^{\mathrm{sha}'}$, while if $x_{\xi'} + \Gamma_{\mathrm{rad}}^{\mathrm{sha}'} \leq x_\xi + \Gamma_{\mathrm{rad}}^{\mathrm{sha}}$, $\mathcal{R}_{\mathrm{wei}}=1$ when $\Psi_{\mathrm{esp}}^t \in [\Upsilon_{t,\min}^{\mathrm{sha}'}, \Upsilon_{t,\min}^{\mathrm{sha}}]^{\mathrm{sha}'} \cup (\Upsilon_{t,\min}^{\mathrm{sha}}, \Upsilon_{t,\max}^{\mathrm{sha}})^{\mathrm{sha}} \cup [\Upsilon_{t,\max}^{\mathrm{sha}}, \Upsilon_{t,\max}^{\mathrm{sha}'}]^{\mathrm{sha}'}$. Only when the value of $\mathcal{R}_{\mathrm{wei}}$ is equal to 1 from the perspective of both the transmitter and receiver, the differential reflection area contributes energy to $\mathcal{Q}_{r,\mathrm{ref}}$.

Furthermore, we also provide the solution steps of $\mathcal{R}_{\mathrm{wei}}$ for multiple obstacle situations. Initially, the circumstances where $\mathcal{R}_{\mathrm{wei}}$ is equal to 1 need to be investigated from the perspective of the receiver. In this step, the relationship among the critical parameters $\Upsilon_{r,\min}^{\mathrm{sha}}$ and $\Upsilon_{r,\max}^{\mathrm{sha}}$ of multiple obstacles need to be discussed, and meanwhile, the Ψ_{esp}^r intervals that the photon's receiving link is not blocked by obstacles need to be provided. Moreover, the circumstances where $\mathcal{R}_{\mathrm{wei}}$ is equal to 1 need to be determined from the perspective of the transmitter. In this step, the relationship among the critical parameters $\Upsilon_{t,\min}^{\mathrm{sha}}$ and $\Upsilon_{t,\max}^{\mathrm{sha}}$ of multiple obstacles require to be investigated, and at the same time, the Ψ_{esp}^t intervals that the photon's transmitting link is not blocked by obstacles require to be presented. Only when $\mathcal{R}_{\mathrm{wei}}=1$ from the perspective of both the transmitter and receiver, the differential reflection area contribute energy to $\mathcal{Q}_{r,\mathrm{ref}}$. During the derivation of $\mathcal{R}_{\mathrm{wei}}$, we default to the fact that the angle between $\boldsymbol{n}_{\xi_a}$ ($\boldsymbol{n}_{\xi_b}$, $\boldsymbol{n}_{\xi_c}$, $\boldsymbol{n}_{\xi_d}$, and $\boldsymbol{n}_{\xi_e}$) and $-\boldsymbol{\varepsilon}$ as well as the angle between $\boldsymbol{n}_{\xi_a}$ ($\boldsymbol{n}_{\xi_b}$, $\boldsymbol{n}_{\xi_c}$, $\boldsymbol{n}_{\xi_d}$, and $\boldsymbol{n}_{\xi_e}$) and $\boldsymbol{\nu}$ are both less than 90 degrees, which can eliminate the possibility of a photon traveling through the obstacle to reach

Authorized licensed use limited to: University of Witwatersrand. Downloaded on November 06,2025 at 14:42:10 UTC from IEEE Xplore. Restrictions apply.

the differential reflection area ds as well as a reflected photon traveling through the obstacle to arrive at the receiver.

It is noteworthy that although a Lambertian-distributed light source (e.g., LED) was adopted for modeling in this article, the applicability of the proposed model can be easily extended to encompass sources with other emission patterns. Specifically, when applying the proposed model to non-Lambertian sources [21], [37], three modifications to the aforementioned modeling procedure are required: 1) replace the emission pattern of the light source in expressions $\mathcal{Q}_{r,\mathrm{sca}}$ and $\mathcal{Q}_{r,\mathrm{ref}}$ with that of the specified non-Lambertian source; 2) update the constraint (10) to $\boldsymbol{\mu}_t\boldsymbol{\varepsilon}^{\mathrm{T}}/\varepsilon \geq \cos\beta_t$, where β_t is the half beam angle of the light source; and 3) consider the constraints of source parameters $\Psi^t_{\max}$ and $\Psi^t_{\min}$ when solving both $\mathcal{S}_{\mathrm{wei}} = 1$ and $\mathcal{R}_{\mathrm{wei}} = 1$ from the viewpoint of the transmitter, where $\Psi^t_{\max}$ and $\Psi^t_{\min}$ denote the maximum and minimum angles, respectively, formed between the rays resulting from the intersection of plane $\mathcal{F}_\sigma$ with the transmitter beam boundary and the reference ray TH.

As for the obstacle region, although we only consider the obstacle circumstances shown in Fig. 2, the applicability of the proposed model can be readily extended to scenarios involving obstacles with regular contours and various numbers based on the proposed modeling procedure. For scenarios involving irregular obstacles, we first approach their contours utilizing regular obstacles. Subsequently, the proposed OBAM is employed for boundary processing. Finally, the modeling is conducted according to the procedure presented above.

Generally, the proposed model applies to short-range UV communication scenarios and requires an overlap volume between the transmitter beam and the receiver FoV. To eliminate these limitations, the MCPT method can be employed for modeling the NLoS UV channels, incorporating the effects of turbulence, especially for long-range scenarios. This is primarily because, as the communication range increases or the overlap volume decreases, the component of multiple scattering to the received pulse energy becomes increasingly considerable. However, this component cannot be captured through the proposed integral method.

V. Numerical Results

In this section, we assess the validity of the proposed model and analyze the impacts of different obstacle situations on the channel properties of NLoS UV communications. According to the existing studies [21], [22], [37], path loss is considered as one of the most important metrics for UV communications and is widely adopted for channel characterization. Since it can enable further investigation into the key communication performance of NLoS UV systems, such as achievable data rate, bit error rate, and effective propagation distance. For these reasons, we select the path loss metric to conduct the relevant simulation analysis. All simulations are performed within the MATLAB R2022b computational environment on a computer equipped with a 2 GHz quad-core Intel Core i5 processor and 16 GB of LPDDR4X RAM.

The validity of the proposed model is investigated in Fig. 5, where the simulation results of the MCPT model are employed as the criterion, and its correctness is experimentally confirmed in two representative scenarios [39]. Besides, the shape of the obstacle is chosen as the RP, and its parameters are set below: μ_c, ω_c, γ_c, x_c, y_c, and α_c are set to $r/10$, $3r$, $3r$, $-\mu_c/2 - 10\,\mathrm{m}$ (or $-\mu_c/2 - 20\,\mathrm{m}$), $r/2$, and 0 degrees, respectively; and the reflection parameters v_r, μ, and m_s are set to 0.1, 0.5, and 5, respectively, which are consistent with those in [39]. Moreover, the number of simulation photons and their survival probability threshold for the MCPT model are set to 10^7 and 10^{-10}, respectively. Concerning the remaining parameter settings, they are presented in Table IV. Numerical results demonstrate that the path loss curves determined by the proposed model agree well with those obtained by the MCPT model, while its simulation time is less than 10% that of the MCPT model. Beyond that, these results reveal that the path loss of the NLoS UV channel without obstacles is larger than that of the channel considering an obstacle at given parameter settings, which is mainly because the contribution of obstacle reflection to $\mathcal{Q}_r$ is more prominent. Furthermore, the variation in the distance between the reflection surface and transceiver FoVs (DBRST) has a significant impact on the overall path loss of NLoS channels. Specifically, when r is small, the smaller the DBRST value, the lower the corresponding channel

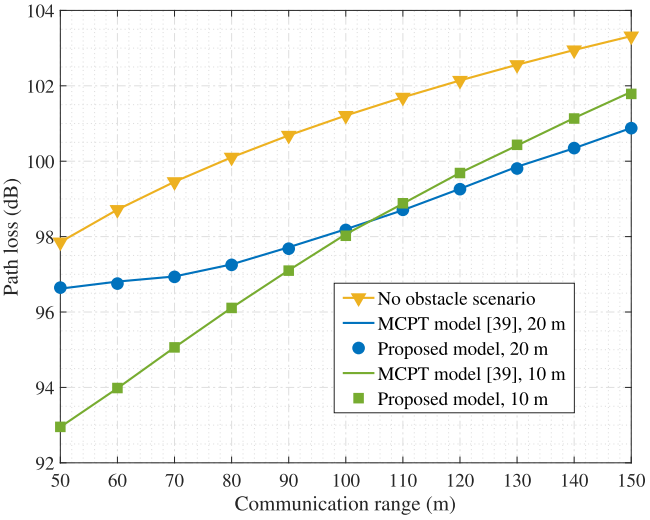


Fig. 5. Path loss comparison of the proposed model and the MCPT model at different obstacle situations.

TABLE IV
Parameter Settings for the Proposed Model and MCPT Model

Parameters	Values	Parameters	Values
k_s^{Ray}	$0.24\,\mathrm{km}^{-1}$	$\beta_{1/2}$	$\pi/6$
k_s^{Mie}	$0.25\,\mathrm{km}^{-1}$	β_r	$\pi/6$
k_a	$0.90\,\mathrm{km}^{-1}$	α_t	$-19\pi/36$
γ	0.017	α_r	$19\pi/36$
g	0.72	ϑ_t	$7\pi/36$
f	0.5	ϑ_r	$7\pi/36$
v_r	0.1	A_r	$1.92\,\mathrm{cm}^2$
μ	0.5	m_s	5

Authorized licensed use limited to: University of Witwatersrand. Downloaded on November 06,2025 at 14:42:10 UTC from IEEE Xplore. Restrictions apply.

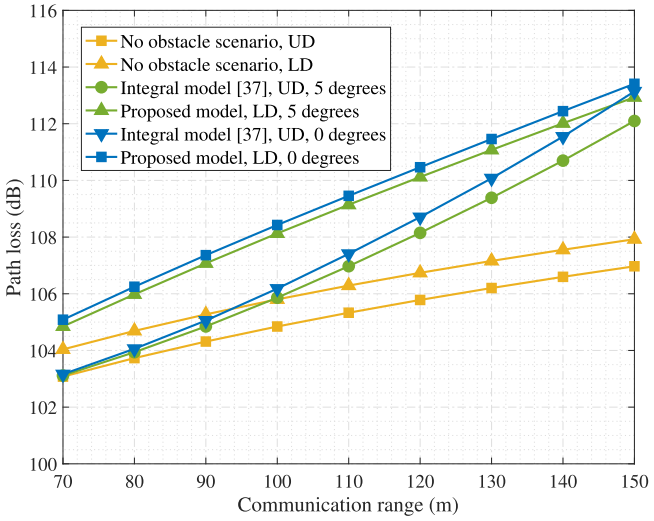


Fig. 6. Path loss results of the scattered energy for the proposed model and the integral model at different obstacle orientation angles.

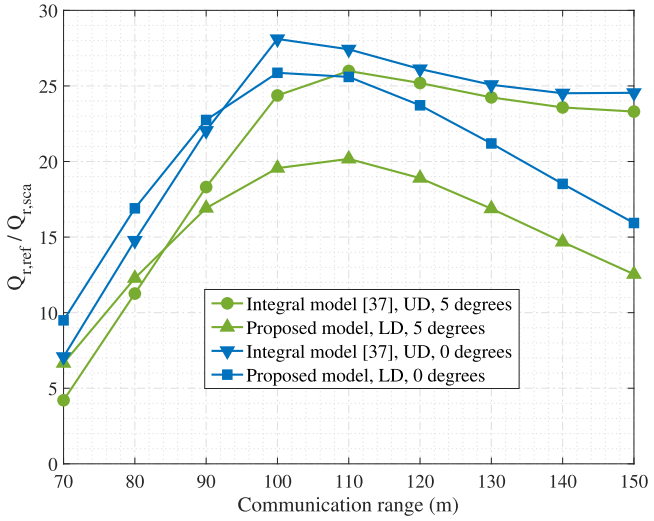


Fig. 7. Ratios of $\mathcal{Q}_{r,\mathrm{ref}}$ to $\mathcal{Q}_{r,\mathrm{sca}}$ for the proposed model and the integral model at different obstacle orientation angles.

TABLE V
PARAMETER SETTINGS FOR THE TRANSCEIVER AND OBSTACLE

Parameters	Values	Parameters	Values
$\beta_{1/2}$	$\pi/12$	ω_c	40 m
β_r	$\pi/12$	γ_c	80 m
α_t	$-2\pi/3$	μ_c	30 m
α_r	$2\pi/3$	α_c	0°, 5°
ϑ_t	$\pi/9$	ϑ_r	$\pi/9$

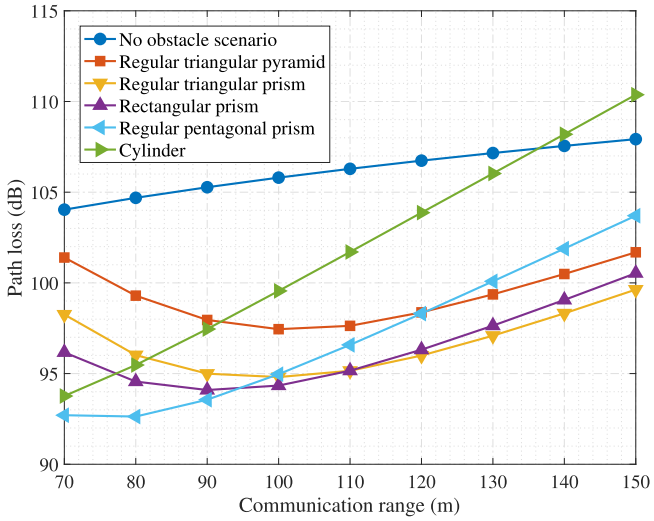


Fig. 8. Path loss results for NLoS UV communication channels incorporating different obstacle shapes.

path loss, while when r is large, the larger the DBRST value, the lower the corresponding channel path loss.

Fig. 6 demonstrates the performance of the proposed OBAM in handling obstacle boundaries. Related parameter settings are summarized in Table V, where x_c and y_c can be expressed as $-\Gamma_{\mathrm{rad}}^{\mathrm{RP}}\sin[\tan^{-1}(\mu_c/\omega_c)+\alpha_c]-\mu_c$ and $r/2$, respectively, and the remaining parameter settings are consistent with Table IV. Regarding UD and LD, they represent the radiation intensity of the light source obeys a uniform distribution and a Lambertian distribution, respectively. Numerical results indicate that under identical source radiation patterns, the path loss for scattered energy in obstacle-free channels is consistently lower than that in obstructed channels, irrespective of the obstacle orientation angle. Further, with all other parameters held constant, the path loss variation induced by radiation pattern differences remains stable at 0.95 dB across varying communication ranges. Thus, the error introduced by the proposed OBAM can be inferred. Specifically, when α_c is set to 0° and 5°, the assessment error ranges attributable to OBAM are [0,1.35] dB and [0,1.30] dB, respectively.

Fig. 7 presents the ratios of $\mathcal{Q}_{r,\mathrm{ref}}$ to $\mathcal{Q}_{r,\mathrm{sca}}$ for the proposed model and the latest work [37] at different obstacle orientation angles, where the related parameter settings are consistent with those in Fig. 6. Numerical results manifest that, under a fixed obstacle orientation angle, the ratio of $\mathcal{Q}_{r,\mathrm{ref}}$ to $\mathcal{Q}_{r,\mathrm{sca}}$ for the LD source channel exceeds that for the UD source channel at shorter communication ranges, while it is lower than that for the UD source channel at longer communication ranges. Apart from this, we observe a phenomenon that the ratio of $\mathcal{Q}_{r,\mathrm{ref}}$ to $\mathcal{Q}_{r,\mathrm{sca}}$ initially increases and subsequently decreases with the increase of communication range. This is mainly because when r is small, the area of the beam at the obstacle is smaller than the area of the obstacle available for reflection, and when r is large, the effective reflection area (ERA) remains constant while the effective scattering volume increases. Combining with Fig. 6, we can conclude that the assessment error ranges attributable to OBAM can be ignored when obstacle reflection is obvious. Specifically, when r and α_c are set to 100 m and 5 degrees, the contribution ratios of $\mathcal{Q}_{r,\mathrm{sca}}$ to $\mathcal{Q}_r$ are only 5% and 4%, respectively, for the proposed model and the integral model.

Moreover, we investigate the impacts of the obstacle shapes on the channel path loss under identical transceiver parameter settings, as shown in Fig. 8. The system model parameters are selected as follows: x_ξ, y_ξ, z_ξ, and $\Gamma_{\mathrm{rad}}^{\mathrm{sha}}$ are set to -46.7 m,

Authorized licensed use limited to: University of Witwatersrand. Downloaded on November 06,2025 at 14:42:10 UTC from IEEE Xplore. Restrictions apply.

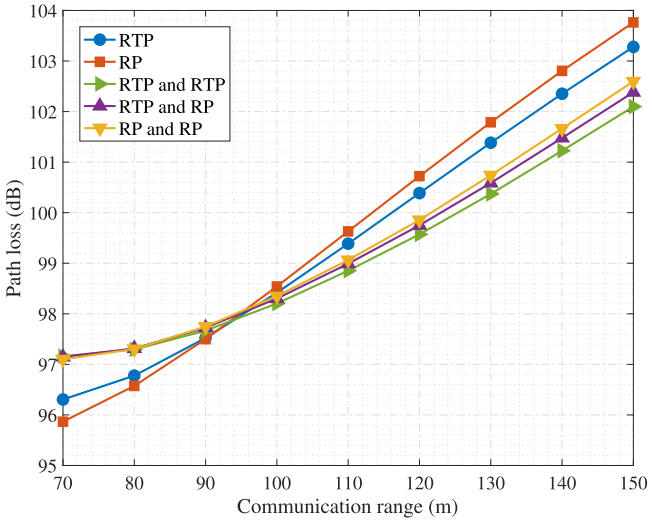


Fig. 9. Path loss comparison for single obstacle situations and double obstacle situations.

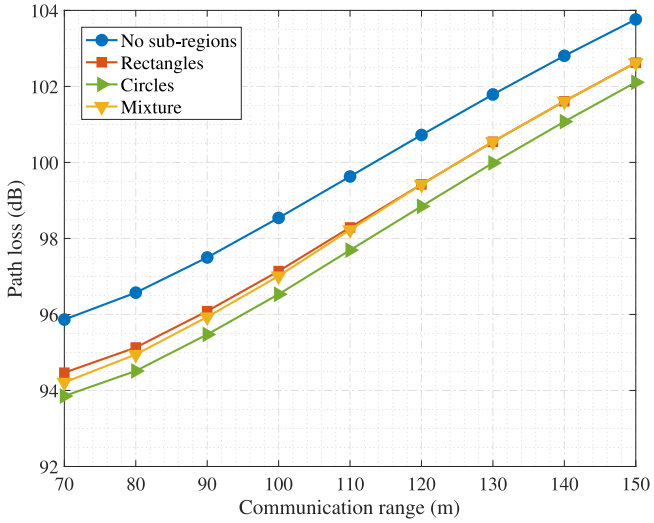


Fig. 10. Path loss results for obstacle reflection surfaces containing multiple subregions with different contours.

TABLE VI
PARAMETER SETTINGS FOR SINGLE AND DOUBLE OBSTACLE SITUATIONS

Parameters	Values	Parameters	Values
$\beta_{1/2}$	$\pi/6$	ω_c	40 m
β_r	$\pi/6$	$\gamma_{b,c}$	80 m
α_t	$-2\pi/3$	μ_c	30 m
α_r	$2\pi/3$	$x_{b,c}$	-46.7 m
ϑ_t	$7\pi/36$	$\Gamma_{\text{rad}}^{rtp}$	25 m
ϑ_r	$7\pi/36$	α_b	$\pi/3$

$r/2$, 80 m, and 25 m, respectively; α_a, α_b, α_c, and α_d are set to $\pi/3$, $\pi/3$, 0, and $\pi/5$, respectively; and the rest parameter settings are the same as those in Table V. Numerical results demonstrate that channels incorporating RTPY, RTP, RP, and RPP exhibit significantly lower path loss compared to obstacle-free channels, whereas channels with CYL show higher path loss than those of obstacle-free channels when r is relatively large. In addition, among these five obstacle shapes, the channel with RPP exhibits the minimum path loss while the channel with RTPY shows the maximum path loss at small r values. Conversely, at large r values, the channel incorporating RTP demonstrates the lowest path loss, whereas the channel with CYL presents the highest path loss.

Fig. 9 presents the path loss for NLoS channels considering single and double obstacle situations. Related transceiver and obstacle parameter settings are provided in Table VI. Numerical results manifest that when the communication range is short, the path loss in the single-obstacle situation is less than that in the two-obstacle situation. However, when the communication range is long, the path loss in the single-obstacle situation is higher than that in the two-obstacle situation. This behavior is primarily tied to the ERA provided by the obstacles. Specifically, when r is small, the area of the beam at the obstacle is much smaller than the ERA provided by the obstacles, which leads to the channel with RP showing the minimum path loss. Since in this situation, increasing the volume of the obstacle will obviously reduce the contribution of air scattering to the received pulse energy. Compared with the combinations of RTP and RTP, RTP and RP, and RP and RP, RP possesses the smallest volume. The reason why the path loss for the channel with RP is lower than that for the channel with RTP is that $\Upsilon_{r,\min}^{\text{RTP}} < \Upsilon_{r,\min}^{\text{RP}}$, and $\Upsilon_{t,\min}^{\text{RTP}} < \Upsilon_{t,\min}^{\text{RP}}$ at small r values, where causes the effective scattering volume for the channel with RP being larger than that for the channel considering RTP. However, when r is large, the area of the beam at the obstacle is larger than the ERA provided by the obstacles, which leads to the combination of RTP and RTP exhibiting the minimum path loss. Since this combination possesses the largest ERA compared with RTP, RP, and the combinations of RTP and RP, and RP and RP. From Fig. 9, it can also be observed that all path loss curves intersect at a single point. This occurs because, at this specific location, the illuminated area of the transmitted beam on the effective reflection surfaces for the five obstacle situations is comparable.

Fig. 10 examines the impacts of different obstacle reflection properties on the channel path loss. For simplicity, the obstacle shape is chosen as a RP, and the system model parameters are configured as follows: $v_{r,in}$, $v_{r,out}$, μ_{in} (μ_{out}), and $m_{s,in}$ ($m_{s,out}$) are set to 0.3, 0.1, 0.5 (0.5), and 5 (5), respectively; w_{uv}, s_{uv}, and r_{uv} are selected as 5, 5, and 3.5 m, respectively; and the remaining parameter settings are consistent with those in Table VI. Moreover, the effective reflection surface is divided into 32 grids, with each grid assumed to contain a single subregion. Numerical results show reduced path loss in scenarios containing subregions compared to those without subregions, attributable to higher reflection coefficient values inside versus outside these subregions. Further, among scenarios containing three types of subregions, the configuration with hybrid circular and rectangular subregions yields the smallest path loss. This is attributed to this scenario having the largest total subregion area.

Authorized licensed use limited to: University of Witwatersrand. Downloaded on November 06,2025 at 14:42:10 UTC from IEEE Xplore. Restrictions apply.

VI. Conclusion

This article proposed a single-collision model for NLoS UV communication channels, where the representative shapes and numbers of obstacles and their different reflection properties are taken into account to approach real IoT environments. Moreover, an OBAM was developed to reduce the modeling complexity. To validate the proposed model, we compared it with the MCPT model and the integral model through numerical results, which prove its correctness and effectiveness. Besides, calculations showed that under identical source radiation patterns, the path loss for scattered energy in the obstacle-free channel is lower than that in the obstructed channel, irrespective of the obstacle orientation angle. Further, when the ratio of reflected energy to scattered energy is large, the assessment errors attributable to the proposed OBAM could be neglected. Beyond that, when the area of the transmitter beam at the obstacle is much smaller than the ERA provided by the obstacle, increasing the illuminated area of the transmitter beam on the ERA could reduce the channel path loss.

References

[1] T. Wu et al., "Path loss modeling for NLoS ultraviolet channels incorporating scattering and reflection effects," 2024, *arXiv:2411.05363*.

[2] R. Yuan and J. Ma, "Review of ultraviolet non-line-of-sight communication," *China Commun.*, vol. 13, no. 6, pp. 63–75, Jun. 2016.

[3] A. Vavoulas, H. G. Sandalidis, N. D. Chatzidiamantis, Z. Xu, and G. K. Karagiannidis, "A survey on ultraviolet C-Band (UV-C) communications," *IEEE Commun. Surveys Tuts.*, vol. 21, no. 3, pp. 2111–2133, 3rd Quart., 2019.

[4] G. Chen, T. Wu, F. Yang, T. Wang, J. Song, and Z. Han, "Ultraviolet-based UAV swarm communications: Potentials and challenges," *IEEE Wireless Commun.*, vol. 29, no. 5, pp. 84–90, Oct. 2022.

[5] S. Arya and Y. H. Chung, "A comprehensive survey on optical scattering communications: Current research, new trends, and future vision," *IEEE Commun. Surveys Tuts.*, vol. 26, no. 2, pp. 1446–1477, 2nd Quart., 2024.

[6] T. Wu, T. Cao, F. Yang, J. Song, J. Cheng, and Z. Han, "Ultraviolet-based indoor wireless communications: Potentials, scenarios, and trends," *IEEE Commun. Mag.*, vol. 62, no. 3, pp. 82–88, Dec. 2023.

[7] Z. Xu and B. M. Sadler, "Ultraviolet communications: Potential and state-of-the-art," *IEEE Commun. Mag.*, vol. 46, no. 5, pp. 67–73, May 2008.

[8] R. J. Drost, T. J. Moore, and B. M. Sadler, "Ultraviolet scattering propagation modeling: Analysis of path loss versus range," *J. Opt. Soc. America A*, vol. 30, no. 11, pp. 2259–2265, Nov. 2013.

[9] Z. Wang, R. Yuan, J. Cheng, and M. Peng, "Joint optimization of full-duplex relay placement and transmit power for multihop ultraviolet communications," *IEEE Internet Things J.*, vol. 11, no. 7, pp. 11960–11973, Apr. 2024.

[10] S. Yu, C. Gong, and Z. Xu, "Design and optimization of sandwich-type synchronization sequence for optical wireless communication with a photon-counting receiver," *IEEE Internet Things J.*, vol. 11, no. 9, pp. 15880–15893, May 2024.

[11] T. Wu, T. Cao, F. Yang, J. Song, J. Cheng, and Z. Han, "Modeling of UV diffused-LoS communication channel incorporating obstacles: an integration perspective," *IEEE Trans. Wireless Commun.*, vol. 23, no. 10, pp. 13515–13529, Oct. 2024.

[12] M. R. Luettgen, J. H. Shapiro, and D. M. Reilly, "Non-line-of-sight single-scatter propagation model," *J. Opt. Soc. Amer. A, Opt. Image Sci.*, vol. 8, no. 12, pp. 1964–1972, Dec. 1991.

[13] M. A. Elshimy and S. Hranilovic, "Non-line-of-sight single-scatter propagation model for noncoplanar geometries," *J. Opt. Soc. America A*, vol. 28, no. 3, pp. 420–428, Mar. 2011.

[14] Y. Zuo, H. Xiao, J. Wu, Y. Li, and J. Lin, "A single-scatter path loss model for non-line-of-sight ultraviolet channels," *Opt. Express*, vol. 20, no. 9, pp. 10359–10369, Apr. 2012.

[15] T. Wu, J. Ma, P. Su, R. Yuan, and J. Cheng, "Modeling of short-range ultraviolet communication channel based on spherical coordinate system," *IEEE Commun. Lett.*, vol. 23, no. 2, pp. 242–245, Feb. 2019.

[16] Z. Shen, J. Ma, T. Shan, and T. Wu, "Modeling of ultraviolet scattering propagation and its applicability analysis," *Opt. Lett.*, vol. 44, no. 20, pp. 4953–4956, Oct. 2019.

[17] Z. Xu, H. Ding, B. M. Sadler, and G. Chen, "Analytical performance study of solar blind non-line-of-sight ultraviolet short-range communication links," *Opt. Lett.*, vol. 33, no. 16, pp. 1860–1862, Aug. 2008.

[18] Y. Zuo, H. Xiao, J. Wu, W. Li, and J. Lin, "Closed-form path loss model of non-line-of-sight ultraviolet single-scatter propagation," *Opt. Lett.*, vol. 38, no. 12, pp. 2116–2118, Jun. 2013.

[19] T. Wu, J. Ma, R. Yuan, P. Su, and J. Cheng, "Single-scatter model for short-range ultraviolet communication in a narrow beam case," *IEEE Photon. Technol. Lett.*, vol. 31, no. 3, pp. 265–268, Feb. 2019.

[20] T. Cao, J. Song, and C. Pan, "Simplified closed-form single-scatter path loss model of non-line-of-sight ultraviolet communications in noncoplanar geometry," *IEEE J. Quantum Electron.*, vol. 57, no. 2, pp. 1–9, Apr. 2021.

[21] H. Ding, G. Chen, A. Majumdar, B. M. Sadler, and Z. Xu, "Modeling of non-line-of-sight ultraviolet scattering channels for communication," *IEEE J. Sel. Areas Commun.*, vol. 27, no. 9, pp. 1535–1544, Dec. 2009.

[22] R. J. Drost, T. J. Moore, and B. M. Sadler, "UV communications channel modeling incorporating multiple scattering interactions," *J. Opt. Soc. Amer. A*, vol. 28, no. 4, pp. 686–695, Apr. 2011.

[23] R. Yuan, J. Ma, P. Su, Y. Dong, and J. Cheng, "Monte-Carlo integration models for multiple scattering based optical wireless communication," *IEEE Trans. Commun.*, vol. 68, no. 1, pp. 334–348, Jan. 2020.

[24] T. Shan, J. Ma, T. Wu, Z. Shen, and P. Su, "Modeling of ultraviolet omni-directional multiple scattering channel based on Monte Carlo method," *Opt. Lett.*, vol. 45, no. 20, pp. 5724–5727, Oct. 2020.

[25] T. Wu, F. Yang, T. Cao, and J. Song, "Modeling of ultraviolet propagation from air to human epidermis with wavelength range of 200–300 nm," *Opt. Lett.*, vol. 47, no. 7, pp. 1662–1665, Apr. 2022.

[26] D. K. Borah, V. R. Mareddy, and D. G. Voelz, "Single and double scattering event analysis for ultraviolet communication channels," *Opt. Express*, vol. 29, no. 4, pp. 5327–5342, Feb. 2021.

[27] R. Yuan, J. Ma, P. Su, and Z. He, "An integral model of two-order and three-order scattering for non-line-of-sight ultraviolet communication in a narrow beam case," *IEEE Commun. Lett.*, vol. 20, no. 12, pp. 2366–2369, Dec. 2016.

[28] J. Tang, T. Lin, C. Gong, and Z. Xu, "Double-scatter characterization on scattering-enhanced non-line-of-sight ultraviolet communication," *IEEE Trans. Commun.*, vol. 73, no. 6, pp. 4335–4348, Jun. 2025.

[29] L. Liao, Z. Li, T. Lang, and G. Chen, "UV LED array based NLOS UV turbulence channel modeling and experimental verification," *Opt. Express*, vol. 23, no. 17, pp. 21825–21835, Aug. 2015.

[30] H. Ding, G. Chen, A. K. Majumdar, B. M. Sadler, and Z. Xu, "Turbulence modeling for non-line-of-sight ultraviolet scattering channels," in *Proc. 8th Atmos. Propag.*, Jan. 2011, pp. 195–202.

[31] B. Li, H. Wang, X. Wu, B. Song, and H. Hu, "Modification of atmospheric extinction coefficient of non-line-of-sight ultraviolet communication under weak turbulence," *Opt. Laser Technol.*, vol. 66, pp. 45–51, Mar. 2015.

[32] T. Shan, J. Ma, T. Wu, Z. Shen, and P. Su, "Single scattering turbulence model based on the division of effective scattering volume for ultraviolet communication," *Chin. Opt. Lett.*, vol. 18, no. 12, pp. 1–5, Dec. 2020.

[33] X. Chu, R. Yuan, and M. Peng, "Turbulent single-scattering channel model for ultraviolet communications using equivalent scattering point approach," *IEEE Commun. Lett.*, vol. 28, no. 7, pp. 1579–1583, Jul. 2024.

[34] R. Yuan and M. Peng, "Single-input multiple-output scattering based optical communications using statical combining in turbulent channels," *IEEE Trans. Wireless Commun.*, vol. 23, no. 4, pp. 2560–2574, Apr. 2024.

[35] G. Chen, Z. Xu, H. Ding, and B. M. Sadler, "Path loss modeling and performance trade-off study for short-range non-line-of-sight ultraviolet communications," *Opt. Express*, vol. 17, no. 5, pp. 3929–3940, Mar. 2009.

[36] L. Wang, Y. Li, Z. Xu, and B. M. Sadler, "Wireless ultraviolet network models and performance in noncoplanar geometry," in *Proc. IEEE Globecom Workshops*, Miami, FL, USA, Dec. 2010, pp. 1037–1041.

[37] T. Wu et al., "Modeling of UV NLoS communication channels: From atmospheric scattering and obstacle reflection perspectives," *IEEE J. Sel. Areas Commun.*, vol. 43, no. 5, pp. 1590–1606, Feb. 2025.

Authorized licensed use limited to: University of Witwatersrand. Downloaded on November 06,2025 at 14:42:10 UTC from IEEE Xplore. Restrictions apply.

[38] T. Wu et al., "Channel modeling for ultraviolet non-line-of-sight communications incorporating an obstacle," in *Proc. IEEE Global Commun. Conf. (GLOBECOM)*, Dec. 2024, pp. 349–354.
[39] T. Cao, X. Gao, T. Wu, C. Pan, and J. Song, "Reflection-assisted non-line-of-sight ultraviolet communications," *J. Lightwave Technol.*, vol. 40, no. 7, pp. 1953–1961, Apr. 2022.
[40] T. Cao, T. Wu, C. Pan, and J. Song, "Single-collision-induced path loss model of reflection-assisted non-line-of-sight ultraviolet communications," *Opt. Express*, vol. 30, no. 9, pp. 15227–15237, Apr. 2022.
[41] H. Zhang, H. Yin, H. Jia, J. Yang, and S. Chang, "Study of effects of obstacle on non-line-of-sight ultraviolet communication links," *Opt. Express*, vol. 19, no. 22, pp. 21216–21226, Oct. 2011.
[42] A. Mohajer, J. Hajipour, and V. C. M. Leung, "Dynamic offloading in mobile edge computing with traffic-aware network slicing and adaptive TD3 strategy," *IEEE Commun. Lett.*, vol. 29, no. 1, pp. 95–99, Jan. 2025.
[43] T. Cao, X. Gao, T. Wu, C. Pan, and J. Song, "Single-scatter path loss model of LED-based non-line-of-sight ultraviolet communications," *Opt. Lett.*, vol. 46, no. 16, pp. 4013–4016, Aug. 2021.
[44] Z. Qian et al., "Size-dependent UV-C communication performance of AlGaN micro-LEDs and LEDs," *J. Lightwave Technol.*, vol. 40, no. 22, pp. 7289–7296, Nov. 2022.
[45] T. Cao et al., "Theoretical and experimental studies on channel impulse response of short-range non-line-of-sight ultraviolet communications" *Opt. Express*, vol. 32, no. 6, pp. 8537–8554, Mar. 2024.
[46] O. González, S. Rodríguez, R. Pérez-Jiménez, B. R. Mendoza, and A. Ayala, "Comparison of Monte Carlo ray-tracing and photon-tracing methods for calculation of the impulse response on indoor wireless optical channels" *Opt. Express*, vol. 19, no. 3, pp. 1997–2005, Jan. 2011.



Tianfeng Wu (Graduate Student Member, IEEE) received the B.S. degree from the College of Instrumentation and Electrical Engineering, Jilin University, Changchun, China, in 2015, and the double master's degree from the Department of Precision Instrument, Tsinghua University, Beijing, China, and the Faculty of Mechanical Engineering, RWTH Aachen University, Aachen, Germany, in 2019. He is currently pursuing the Ph.D. degree with the Department of Electronic Engineering, Tsinghua University.

He received a Deutscher Akademischer Austausch Dienst (DAAD) scholarship from 2015 to 2016. His research interests include optical scattering communications and channel modeling.



Fang Yang (Senior Member, IEEE) received the B.S.E. and Ph.D. degrees in electronic engineering from Tsinghua University, Beijing, China, in 2005 and 2009, respectively.

He is currently an Associate Professor with the Department of Electronic Engineering, Tsinghua University. He has published over 180 peer reviewed journal and conference papers. He holds over 50 Chinese patents and two PCT patents. His research interests are in the fields of optical wireless communication, wireless communication, intelligent reflecting surface-aided communication.

Dr. Yang received the IEEE Scott Helt Memorial Award (best paper award in IEEE Transactions on Broadcasting) in 2015. He is a Fellow of IET.



Tian Cao (Member, IEEE) received the B.S. and M.S. degrees in telecommunication engineering from Xidian University, Xi'an, China, in 2014 and 2017, respectively, and the Ph.D. degree from the Department of Electronic Engineering, Tsinghua University, Beijing, China, in 2023.

He is currently working as a Lecturer with the School of Telecommunications Engineering, Xidian University. His research interests include ultraviolet communications and visible light communications.



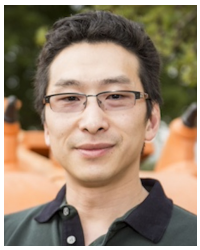
Renzhi Yuan (Member, IEEE) received the B.S. degree in mechanical engineering from Tongji University, Shanghai, China, in 2011, the M.S. degree in precision instrument from Tsinghua University, Beijing, China, in 2017, and the Ph.D. degree in electrical engineering from the University of British Columbia, Kelowna, BC, Canada, in 2021.

He is currently a Distinguished Research Fellow with the School of Information and Communication Engineering and the State Key Laboratory of Networking and Switching Technology, Beijing University of Posts and Telecommunications, Beijing. His research interests include the space-air-ground integrated communications, wireless optical communications, and quantum communications.



Li Fei received the master's and Ph.D. degree in information and communication engineering from Beihang University, Beijing, China, in 2010 and 2015, respectively.

He currently works with Hanjiang National Laboratory, Wuhan, China, as a Research Fellow, and mainly engaged in the wireless communications, optical communications, and marine communications.



Ling Cheng (Senior Member, IEEE) received the B.Eng. (cum laude) degree in electronics and information from Huazhong University of Science and Technology (HUST), Wuhan, China, in 1995, the M.Ing. degree in electrical and electronics (cum laude) and the D.Ing. degree in electrical and electronics from University of Johannesburg (UJ), in 2005 and 2011, respectively.

In 2010, he joined University of the Witwatersrand, Johannesburg, South Africa, where he was promoted to Full Professor in 2019. He has been a visiting professor with five universities and the principal advisor for over forty full research postgraduate students. He has published more than one hundred research papers in journals and conference proceedings. His research interests are in telecommunications and artificial intelligence.

Prof. Cheng was awarded the Chancellor's medals in 2005, 2019 and the National Research Foundation ratings in 2014, 2020. The IEEE ISPLC 2015 best student paper award was made to his Ph.D. student in Austin. He serves as an associate editor of three journals. He is the Vice-Chair of IEEE South African Information Theory Chapter.



Jian Song (Fellow, IEEE) received the B.Eng. and Ph.D. degrees in electrical engineering from Tsinghua University, Beijing, China, in 1990 and 1995, respectively.

He is currently the Director of Tsinghua DTV Technology Research and Development Center, Tsinghua University. He has been working in quite different areas, including fiber-optic, satellite, and wireless communications, as well as the power-line communications. He holds two U.S. and more than 80 Chinese patents. He has published more than 300 peer-reviewed journal and conference papers and coauthored several books in the aforementioned areas. His current research interest is in the area of digital TV broadcasting, network convergence, and visible light communication networks.

Dr. Song won several awards both international and domestic. He is also Fellow of IET, Chinese Institute of Electronics, and Chinese Institute of Communications.

Authorized licensed use limited to: University of Witwatersrand. Downloaded on November 06,2025 at 14:42:10 UTC from IEEE Xplore. Restrictions apply.



Julian Cheng (Fellow, IEEE) received the B.Eng. degree (Hons.) in electrical engineering from the University of Victoria, Victoria, BC, Canada, in 1995, the M.Sc. degree in mathematics and engineering from Queen's University, Kingston, ON, Canada, in 1997, and the Ph.D. degree in electrical engineering from the University of Alberta, Edmonton, AB, Canada, in 2003.

He is a Full Professor with the School of Engineering, Faculty of Applied Science, The University of British Columbia, Kelowna, BC, Canada. He is a Registered Professional Engineer in British Columbia, Canada. He was with Bell Northern Research and NORTEL Networks. His research interests include machine learning and deep learning for wireless communications, wireless optical technology, and quantum communications.

Dr. Cheng served as the President of the Canadian Society of Information Theory from 2017 to 2021. He was the Co-Chair of the 12th Canadian Workshop on Information Theory in 2011, the 28th Biennial Symposium on Communications in 2016, and the General Co-Chair of the 2021 IEEE Communication Theory Workshop. He is the Chair of the Radio Communications Technical Committee of the IEEE Communications Society. He was a past Associate Editor of the IEEE TRANSACTIONS ON COMMUNICATIONS, the IEEE TRANSACTIONS ON WIRELESS COMMUNICATIONS, the IEEE COMMUNICATIONS LETTERS, and the IEEE ACCESS, as well as an Area Editor for the IEEE TRANSACTIONS ON COMMUNICATIONS. He served as a Guest Editor for a Special Issue of the IEEE JOURNAL ON SELECTED AREAS IN COMMUNICATIONS on *Optical Wireless Communications*.



Zhu Han (Fellow, IEEE) received the B.S. degree in electronic engineering from Tsinghua University, Beijing, China, in 1997, and the M.S. and Ph.D. degrees in electrical and computer engineering from the University of Marylandat College Park, College Park, MD, USA, in 1999 and 2003, respectively.

From 2000 to 2002, he was an Research and Development Engineer of JDSU, Germantown, MD, USA. From 2003 to 2006, he was a Research Associate with the University of Maryland. From 2006 to 2008, he was an Assistant Professor with Boise State University, Boise, ID, USA. He is currently a John and Rebecca Moores Professor with the Electrical and Computer Engineering Department as well as in the Computer Science Department, the University of Houston, Houston, Tx, USA. His main research targets on the novel game-theory related concepts critical to enabling efficient and distributive use of wireless networks with limited resources. His other research interests include wireless resource allocation and management, wireless communications and networking, quantum computing, data science, smart grid, carbon neutralization, and security and privacy.

Dr. Han received an NSF Career Award in 2010, the Fred W. Ellersick Prize of the IEEE Communication Society in 2011, the EURASIP Best Paper Award for the Journal on Advances in Signal Processing in 2015, the IEEE Leonard G. Abraham Prize in the field of Communications Systems (best paper award in IEEE JSAC) in 2016, the IEEE Vehicular Technology Society 2022 Best Land Transportation Paper Award, and several best paper awards in IEEE conferences. He was an IEEE Communications Society Distinguished Lecturer from 2015 to 2018 and ACM Distinguished Speaker from 2022 to 2025, AAAS fellow since 2019, and ACM Fellow since 2024. He is a 1% Highly Cited Researcher since 2017 according to Web of Science. He is also the winner of the 2021 IEEE Kiyo Tomiyasu Award (an IEEE Field Award), for outstanding early to mid-career contributions to technologies holding the promise of innovative applications, with the following citation: "for contributions to game theory and distributed management of autonomous communication networks."

Authorized licensed use limited to: University of Witwatersrand. Downloaded on November 06,2025 at 14:42:10 UTC from IEEE Xplore. Restrictions apply.